An Analysis of Energy Balance in a Helicon Plasma Source for Space Propulsion

by

Justin Matthew Pucci

B.S., Aerospace Engineering, Arizona State University, 2003

Submitted to the Department of Aeronautics and Astronautics
in partial fulfillment of the requirements for the degree of

Master of Science in Aeronautics and Astronautics

at the

MASSACHUSETTS INSTITUTE OF TECHNOLOGY

May 2007

Author .....
Department of Aeronautics and Astronautics
May 25, 2007

Certified by .....
Manuel Martínez-Sánchez
Professor of Aeronautics and Astronautics
Thesis Supervisor

Accepted by .....
Jaime Peraire
Professor of Aeronautics and Astronautics
Chair, Committee on Graduate Students

An Analysis of Energy Balance in a Helicon Plasma Source for Space Propulsion

by

Justin Matthew Pucci

Submitted to the Department of Aeronautics and Astronautics
on May 25, 2007, in partial fulfillment of the
requirements for the degree of
Master of Science in Aeronautics and Astronautics

Abstract

This thesis covers work done on the mHTX@MIT helicon source as it relates to the analysis of power losses. A helicon plasma is a rather complex system with many potential loss mechanisms. Among the most dominant are optical radiation emission, wall losses due to poor magnetic confinement, and poor antenna-plasma coupling. This work sought to establish a first-order breakdown of the loss mechanisms in the mHTX@MIT helicon source so as to allow for a better understanding of the issues effecting efficiency. This thesis proposes the use of a novel thermocouple array, standard plasma diagnostics, and a simple global energy balance model of the system to determine greater details regarding the losses incurred during regular operation. From this it may be possible, by comparing the heat flux on the tube to the applied magnetic field profile, to gain some insight into the effects of magnetic field geometry on the character of the helicon discharge.

Thesis Supervisor: Manuel Martínez-Sánchez
Title: Professor of Aeronautics and Astronautics

Acknowledgments

I would like to express my sincere appreciation and gratitude to my advisor, Professor Manuel Martínez-Sánchez for his guidance throughout this degree. He has provided me with a great deal of knowledge and has taught me how to think more clearly and logically about every situation I encounter as an engineer. Manuel, your sincere curiosity in seemingly every aspect of our work is inspiring to me and will continue to push me to broaden my knowledge in every way possible.

I would also like to thank my second advisor and good friend, Dr. Oleg Batishchev for always being available to discuss the simplest or most complex of topics regardless of the time, and for providing constant support and encouragement, even when I thought there was no real way to tackle the given problem.

My thanks go out to Dr. Jean-Luc Cambier of the US Air Force Research Laboratory/PRSA at Edwards AFB for his continuing support through AFRL/ERC subcontract RS060213-Mini-Helicon Thruster Development. Also thanks to Dr. Mitat Birkan of the US Air Force Office of Scientific Research for equipment provided through the Defense University Research Instrumentation Program (DURIP) Grant. I would also like to express my gratitude to the National Science Foundation Graduate Research Fellowship Program for their full financial support of my education here at MIT. Without their fellowship, this degree may not have come to fruition.

To my helicon lab mates: Nareg and Murat. Thank you so much for being there for all the frustrating times we shared in the lab when things looked as if they couldn't get any worse, and for the constant stream of comic relief sometimes necessary to make it through the day. Our friendships mean a lot to me and I hope that they will continue whether personally or professionally. Thank you to my office mates and good friends, Tanya and Felix for your help through the multiple years of classes, exams, homework, and thesis writing. I couldn't have done it without you guys and your constant encouragement and support.

Finally, I would not only like to give my thanks but to dedicate this thesis to

my family, who have lived everyday of this great experience through my constant communication with them and have made this document possible. Thanks to my father, Ralph for his support and inspiration as well as those great, albeit wordy pep talks. Thanks to my mother, Kathy, who always knows how to kick me into gear and is there for me no matter what and at anytime, be it day or night. To my little sister, Dani: You've been a great friend and a good influence on me during my career here at MIT and for that I thank you. Lastly, but by no means least, to my wife, Marnie, who has shared with me the ups and downs, the trials and tribulations, the good days and the bad days with me every step of the way through this adventure. Your undying support, compassion, and love is what keeps me going everyday of my life and is what has labored to instill in me the strength to finish this degree.

Contents

List of Figures

List of Tables

Chapter 1

Introduction

Space propulsion is a mature, but dynamic field where the state-of-the-art is always being redefined. The complexity of a typical space propulsion system requires interdisciplinary studies and relies on a number of experts in different areas to fully understand and synthesize new technology. While many concepts have been studied rigorously and have been used in space applications for many years, there still exist some newer, less-understood technologies.

1.1 Space Propulsion

Space propulsion can be separated into two main categories: chemical systems and electric systems. Chemical systems utilize the energy stored in the bonds of the propellant to produce a high temperature, high pressure working fluid that can then be expelled from a conventional, converging-diverging nozzle to produce thrust. The major concepts within this area are solid propellants, liquid-bipropellants, monopropellants, and cold-gas thrusters. All of these engines have been successfully implemented on many missions ranging from on-orbit trajectory corrections and drag make-up of satellites to interplanetary science probes. These technologies have been developed very thoroughly in the past half century and benefit from that heritage in the consideration for placement on current and future missions.

The second category, electric propulsion, uses electrical energy to produce an ionized gas or plasma, which then can be accelerated from the engine using a variety of electrothermal, electrostatic, or electromagnetic mechanisms. The most well-understood and best implemented of these concepts is the ion thruster. This thruster relies on a conventional ionization source such as a direct current (DC) arc discharge to ionize the propellant gas, which is then accelerated electrostatically via an array of grids at varying potentials. This is an example of an electrostatic concept because it uses a static electric field to accelerate the working fluid. There are also electrothermal thrusters, which use a DC arc discharge or heating coil to super-heat the gas in preparation for expulsion through a conventional nozzle. Finally, there are electromagnetic thrusters, which ionize the propellant gas in much the same way as the electrostatic concepts, but utilize magnetic fields as part of the acceleration mechanism.

At this point, the reader should have a better appreciation for the difficulty in choosing from one of the many propulsion concepts to service a given mission. This is why a space propulsion engineer must have an intimate understanding of the advantages and disadvantages of each of these technologies. As was previously mentioned, chemical systems have the advantage of being well tested and characterized in the laboratory and in space. However, one of the main disadvantages of chemical propulsion systems is that there is a upper limit on the maximum specific impulse that can be achieved. The specific impulse of a propulsion system can be expressed as the thrust produced per unit mass flow rate of propellant:

$$I_{sp} = \frac{T}{\dot{m} g_0} \tag{1.1.1}$$

Where T is the thrust produced at a given mass flow rate $\dot{m}$ and g_0, the gravitational acceleration of Earth, is used to make specific impulse have units of seconds. Specific impulse is one of the main performance parameters used by engineers to compare propulsion concepts and can be thought of as a measure of efficiency of a particular

Concept	$\mathbf{I_{sp}}$(s)
cold gas	50 - 250
monopropellant	125 - 250
solid propellant	250 - 300
bipropellant	200 - 450
electrothermal	500 - 1000
electromagnetic	1000 - 5000
electrostatic	2000 - 20000

Table 1.1: Typical values of specific impulse for various chemical and electric propulsion concepts.

propellant. Table 1.1 shows the ranges of specific impulse of the abovementioned concepts. Notice that these propulsion systems span four orders of magnitude in specific impulse. This allows the propulsion engineer a great deal of flexibility in the choice of concept to be employed on a given mission; however, it also makes the design process a long and difficult one unless there are clear constraints or requirements.

Another, perhaps, more telling figure of merit used to evaluate the performance of a particular engine or thruster is that of the thrust or internal efficiency. This is a measure of the efficiency of a concept to convert the input energy, whether chemical or electrical, into useful, thrust-producing energy. This can be expressed as

$$\eta = \frac{\frac{T^2}{2\dot{m}}}{P_{input}} \tag{1.1.2}$$

Where, the term in the numerator is the exhaust or kinetic power and is the component that directly produces thrust and $\dot{m}$ is the propellant mass flow rate. Also, for chemical propulsion systems, $P_{input} = \dot{m}H_{reaction}$ and represents the total chemical power stored in the the bonds of the propellant mixture as the product of the propellant mass flow rate, $\dot{m}$ and the heat of reaction of the combustion process, $H_{reaction}$. Finally, for electric propulsion systems, $P_{input} = IV$ and represents the total electric power cast as the product of the current and voltage of the power supply [1].

The internal efficiency is a rather practical measure, as it includes all losses incurred from the point of initial energy input to the final expulsion of the working

fluid from the engine or thruster. This includes losses due to incomplete combustion or finite enthalpy in the exhaust stream in the case of chemical systems or wall losses, excitation collisions, and multiple ions in electric thrusters. While, from a practical standpoint, what happens in between is of little or no interest to the end-user, it is of utmost importance to propulsion researchers. If the nature of the loss mechanisms can be resolved, then there is a possibility that certain measures can be taken to reduce or eliminate them, thus increasing the efficiency of the system. To that end, many aspects of a given propulsion system can be examined in an attempt to resolve and subsequently eliminate specific loss mechanisms; however, a simple model is always the best place to begin.

1.2 Helicon Plasma Sources

Helicon waves are a special case of the right-hand circularly polarized (RCP) electromagnetic wave in that they propagate only in bounded magnetized media. The helicon wave was found in 1960 by Aigrain during his study of waves in solid metals [3]. He observed waves in slabs of super low-temperature sodium that propagated in the range of frequencies $\omega_{ci} \ll \omega \ll \omega_{ce}$, where ω_{ci} is the ion cyclotron frequency and ω_{ce} is the electron cyclotron frequency. Upon further study, he determined that the wave magnetic field vector traced a helix at a fixed time, hence the name "helicon."

Modern helicon plasmas are produced in cylindrical geometries with a DC magnetic field applied along the longitudinal axis [3, 4]. The gas is first weakly ionized by the electrostatic fields in the antenna region as in a typical capacitively- (CCP) or inductively-coupled plasma (ICP). However, upon application of the external magnetic field, the plasma discharge changes character in that it is no longer subject to the skin depth constraint to which the aforementioned CCP and ICP are. This allows the helicon wave to penetrate into the core of the plasma column. The plasma is then further ionized due to a wave-particle interaction and is thought to be aided by a mode conversion at the wall boundary.

Today, helicon wave sources are being used for a variety of applications due to their ability to efficiently produce a uniform, high density plasma. For example, Chen et. al. [5] have produced helicon plasmas with densities up to 10^{18} m^{-3} with uniformities of $\pm 3\%$ for use in materials processing devices. A helicon source is being used as the primary ionization source in the Variable Specific Impulse Magnetoplasma Rocket (VASIMR) concept currently being developed at NASA Johnson Space Center [6, 7, 8]. Jacobson et. al. [9] have been able to routinely produce hydrogen, deuterium, and helium plasmas with peak densities of 10^{19} m^{-3} with the VASIMR helicon source.

Helicon sources have many advantages over conventional plasma sources. First and foremost, they are the most efficient laboratory sources of plasma currently known. The reason for their high efficiency is still a much debated topic; however, it seems to be related to the mechanism by which the wave energy is transferred to the plasma. They also have the ability to produce relatively dense plasmas in the range of 10^{18} m^{-3} 10^{21} m^{-3}. Another very important advantage, particularly in materials processing applications, is the fact that there are no electrodes in contact with the plasma, thus eliminating the possibility of contamination via sputtering. This, of course, is common to all RF plasma sources.

1.3 Overview of Research

The work presented in this thesis seeks to determine the internal efficiency of the mHTX@MIT helicon plasma source as a precursor for propulsion concept studies. That is to say, that the a global energy balance will be performed in an effort to quantify the losses present in the system and their relative proportions. This includes losses incurred due to antenna-plasma coupling inefficiencies, radiation, and magnetic confinement as well as the energy lost to the plume.

This is done by using a simplified model of the system whereby the energy balance is made between the RF power input, the radiation and confinement losses, and the plume losses. It will be shown that for purposes of experimental determination of both

the radiation and confinement losses, it is a reasonable approximation to assume that both losses are sufficiently absorbed by the plasma source tube material to simply diagnose the energy incident on the inner surface of the tube without differentiation between mechanisms.

Chapter 2 gives a brief overview of the experimental facilities that were to be used in conducting this research including the vacuum system, control system, and the radio frequency (RF) power system as well as a brief discussion of the source operation and corresponding observations. Chapter 3 discusses plume diagnostics fundamentals including the general operation and theory governing Langmuir probes, Faraday probes, and Retarding Potential Analyzers (RPA). Chapter 4 reviews heat conduction theory with an extension to the simple method used to determine losses to the plasma source tube. Chapter 5 develops the model used to build the energy balance of the mHTX@MIT helicon system. Finally, Chapter 6 covers recommendations for future work.

Appendix A is a rather detailed overview of helicon wave theory as it is currently understood and covers a full derivation of the helicon wave equation including the various modes and the effects of boundary conditions. This should serve as a basis upon which future theoretical and computational work can be launched as well as a primer for those new to helicon plasma physics. Appendix B discusses a simple helicon fluid model that was developed at the beginning of this work, when computation was still a priority. It is complete insofar as it presents a simple drift-diffusion model that matches those used by other researchers as a starting point for helicon simulation. It includes a description of both the ion and electron fluid equations as well as the antenna current model and simple boundary conditions that provide closure of the system. It is meant to orient the reader towards thinking in terms of helicon plasma simulation, although it should not be taken as a complete or valid model without further study. The author leaves further computational development to those who will take up the responsibility of helicon simulations in the future of the mHTX@MIT program. Appendix C describes the process by which a helicon source and antenna

can be designed using a simple extension of the helicon dispersion relation derived in Appendix A. This method is based largely on theory given by Chen et. al. [3, 4, 5, 10, 15] and has been employed in the design of the mHTX@MIT helicon source. The author cautions the reader that it is merely a proposed method and has not been validated in any broad way; however, it may be used as a baseline for source and antenna design, whilst keeping in mind the controversial nature of current helicon theory and the tenuous understanding of the physical mechanisms governing helicon plasma source operation. Finally, Appendix D gives a brief overview of the methods used to bond the surface-mounted thermocouples to the source tube including details epoxy preparation and curing.

Chapter 2

The mHTX@MIT Facility

The Mini-Helicon Thruster Experiment (mHTX) at MIT's Space Propulsion Laboratory (SPL) is a new program that seeks to establish a firm understanding of the theory and applications of the helicon plasma source as a competitive space propulsion concept. The helicon plasma source, used as an electrothermal thruster, is believed to have the ability to produce moderate thrust levels at moderate to high specific impulses using a variety of different gases [14]. Thrust can also be varied easily by adjusting the mass flow rate of the propellant gas. The helicon source is used because it offers high plasma densities ($10^{13} - 10^{14}$ cm^{-3}) and efficiencies at relatively low powers ($\sim$1 kW).

The system consists of a pair of electromagnets surrounding a quartz tube, in which the plasma is confined. Around this quartz tube and between the two electromagnets, there is a helical antenna that is powered by a radio frequency (RF) power supply. This entire setup is enclosed within a vacuum chamber. The propellant gas is fed to a 2-cm diameter quartz tube through the vacuum chamber wall via a digitally-controlled flow meter. Optical and electrical ports on the chamber walls provide access to the experiment for various diagnostics. The details of each of the above-mentioned systems will be discussed in the sections that follow.

2.1 Vacuum Chamber

The SPL vacuum chamber, affectionately known as AstroVac, is a cylindrical system measuring 1.5 m in diameter and 1.6 m in length. It has six 8 inch ports, four 2-3/4 inch ports, and eight 1-1/4 inch ports, providing maximum flexibility in terms of number and placement of vacuum feedthroughs and optical viewing ports. The chamber is bakeable and is equipped with a mechanical roughing pump and two cryopumps capable of a maximum throughput of 7000 L/s Xenon, which makes possible an ultimate pressure of below 10^{-8} Torr. The entire mHTX experimental setup is contained within AstroVac so that all components are under vacuum while running tests. This provides the ability to measure thrust in the future.

2.2 Magnet System

The magnets used to produce the external magnetic field in a helicon discharge are of utmost importance in determining the behavior of a particular design and, as such, need to be designed in such a way that a wide range of field intensities and shapes can be achieved. The mHTX magnet system is composed of two to three electromagnets wound from 10 AWG square, insulated magnet wire. The magnets are powered by two to three, 35-A, 350-V power supplies and are controlled via the main SPL computer system. These magnets are held in place via four tie rods which have removable spacers, allowing the spacing between the magnets to be varied if field shaping is desired. The default spacing is that necessary to produce a Helmholtz array, thus ensuring a uniform field in the antenna region of the helicon source.

The magnet system is capable of producing a continuous field intensity of approximately 1800 G at a current of 35 A per coil and can be precisely controlled between zero and 1800 G. Due to the high power of these magnets and the fact that they are designed to operate at high vacuum, they have been instrumented with two thermocouples per coil so that their internal temperatures can be monitored. This gives the user a measure of how much longer the system can be run before needing to be cooled

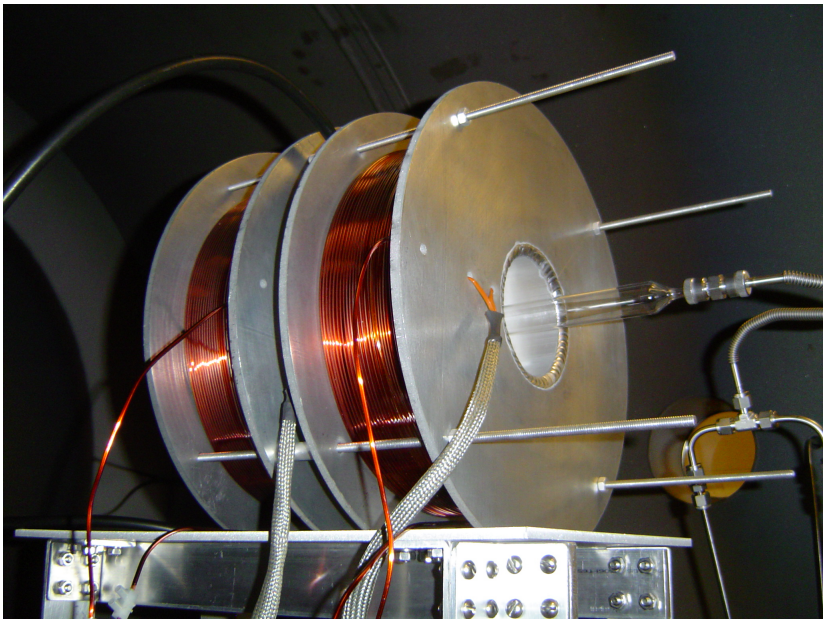

Figure 2-1: Two of the three electromagnets are mounted in a Helmholtz pair configuration. Notice the four tie rods with spacers in between the coils. Also, the shielded, orange thermocouple leads are clearly visible on the right magnet coil. As can be seen, the quartz tube is suspended inside the magnet cores and is attached to the gas feed system at the upstream (right) end.

by way of venting the chamber to atmosphere. Figure 2-1 shows the magnet system with two of the three magnets set up in a Helmholtz pair configuration.

2.3 RF Power System

The RF power system consists of an Advanced Energy RFPP-10 1.2 kW power supply operating at 13.56 MHz, an impedance-matching network, a 13.56 MHz vacuum power feedthrough, a vacuum transmission line, and finally the helicon antenna. This system is rather complex and requires a fair amount of care and attention on a regular basis to ensure that all conductors are making proper contact and that continuity is maintained. Since the power supply, vacuum feedthrough, and transmission line are standard equipment, the details of their design and operation will not be mentioned.

2.3.1 Impedance Matching Network

The impedance-matching network is the most important component in the RF power system. It was designed based on the classic L-network circuit structure and employs two tuneable, vacuum capacitors: one in series and one in parallel with the load (in this case, the antenna and plasma). The need for such a device comes from the fact that the plasma load is dynamic in nature and, as a result, it is necessary to be able to tune the impedance "seen" by the RF power supply to minimize reflected power, thus maximizing the power transmitted to the load. This tuning is done in realtime due to the fact that, during any given test run, parameters such as flow rate, power, or magnetic field intensity may be varied, thus changing the impedance of the discharge. This tuning is performed manually using an oscilloscope, which allows the voltage waveform in the circuit to be measured. The tuner makes adjustments to the capacitance values such that the amplitude of the measured waveform is maximized for a given set of experimental parameters.

2.3.2 Antenna Design

A variety of antenna designs have been employed over the many years of helicon research with varying results [10, 15]. The classic, helical antenna is among the most well characterized and widely used designs [20]. The reader is referred to Figure 2 for details of the physical geometry of a typical helical antenna as it is used in mHTX. Helical antennas come in two varieties: left-handed and right-handed. This nomenclature refers to the direction of rotation of the antenna legs as seen with respect to the wavevector, $\mathbf{k}$. These directionalities also specify the wave mode, where the left-handed and right-handed preferentially excite $m = -1$ and $m = +1$ azimuthal modes, respectively.

To avoid confusion, the reader should note that the twist direction of the antenna and the direction of rotation of the waves are not the same. The left-handed and right-handed helicon waves are based on the direction of rotation of the wave magnetic field

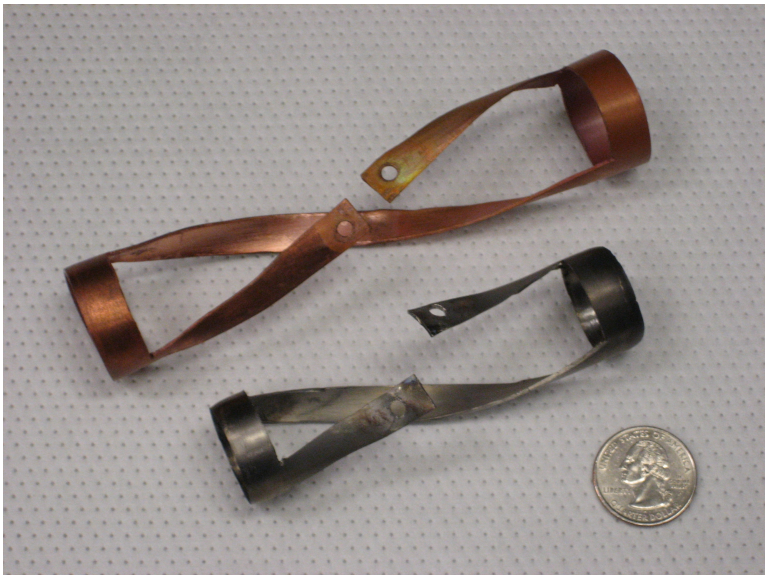

Figure 2-2: Two of the mHTX helical antennas are shown. Both are right-handed and excite the $m = +1$ mode. The resonant energies are 20 eV and 40 eV for the small steel antenna and the large copper antenna, respectively. Different materials were used in these two antennas to rule out the possibility of the existence of a copper emission line, which was thought to be captured during one of the spectroscopy measurements.

vector with respect to the externally applied magnetic field. As such, the direction of the external magnetic field need only be reversed for a given helical antenna design to change the mode that is excited. While either antenna will excite both modes, the $m = +1$ mode has been found to propagate with a greater intensity than the $m = -1$ mode [15].

The antenna used in the mHTX thus far, was designed as a right-handed ($m = +1$), helical antenna with a radius of 1 cm, per the quartz tube size. It is thought that Landau damping is the primary mode of energy transfer between the wave and plasma. It is possible to design the antenna based on this concept. Since, in the case of Landau damping, wave energy is transferred to particles that are near the phase velocity, an antenna can be designed to launch waves of a desired axial phase velocity, $v_p = \omega/k_z$, which is related to the resonant energy, E_r by $E_r = 1/2mv_p^2$. By choosing this energy to be on the order of the peak ionization cross-section energy, the resonant electrons will absorb sufficient energy from the wave to produce ionization

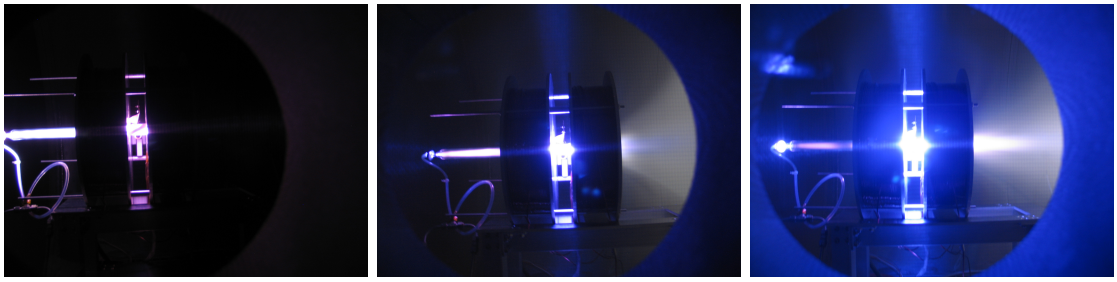

Figure 2-3: Operation with 20 sccm Ar gas flow: (left) - ICP mode, no plume; (center) - intermediate mode with a diffuse plume, and (right) - bright, helicon mode forming a narrow plasma beam at 600 W.

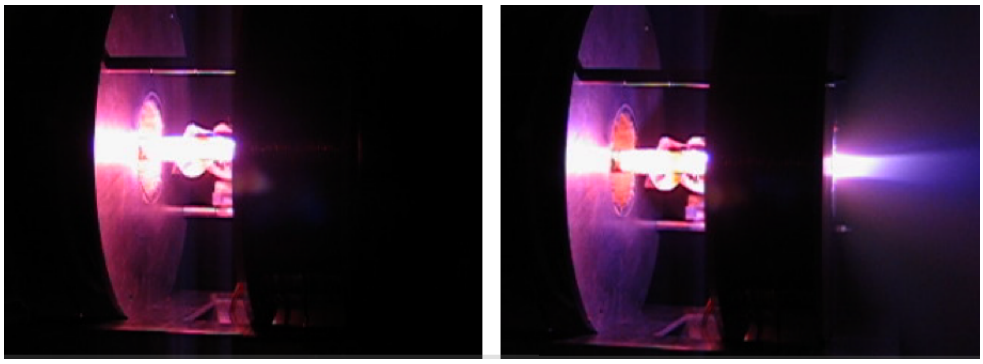

Figure 2-4: Operation with N_2 at 800 W of RF power: (left) - ICP mode with no externally-applied magnetic field, and (right) - Helicon mode with 20 A of magnet current, corresponding to an applied field of 1200 G.

events [10]. Following this line of reasoning, the mHTX antenna has been designed by setting the RF power frequency, ω and choosing an antenna length, L ($k = \pi/L$ for a half-wavelength antenna) equal to that which is necessary to produce a resonant energy on the order of that of the propellant gas. In the case of Argon, resonant energies of 20 eV and 40 eV were selected.

2.4 Operation

Experimental results with argon (Ar) gas operation have been truly encouraging. An RF power of 400 - 1200 W was able to be delivered to the antenna with minimal reflected power. The flow rate was varied between 10 - 100 sccm. In figure 2-3,

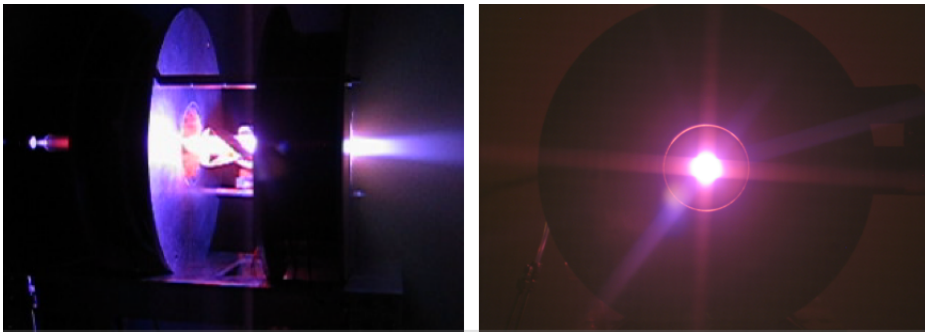

Figure 2-5: Operation at 1200 G with a flow rate of 30 sccm: (left) - 70-percent - 30-percent N_2/Ar mixture (viewed from side), and (right) - an atmospheric air discharge (view is directly into the plasma plume).

three distinct modes of operation are visible. An ICP discharge was observed for a magnetic field intensity below 800 G, an intermediate mode was observed for magnetic field intensities in the range of 800 - 1300 G, and the blue helicon mode was excited above 1300 G. It can be seen that there is a collimated ion beam (blue color from 430 - 480 nm ion emission) ejected axially from the discharge [11, 12, 13].

In addition to Ar, which was the primary propellant during initial testing, the behavior of the discharge in molecular nitrogen (N_2) was studied extensively. Both ICP and helicon modes have been achieved as shown in figure 2-4. A narrow plasma beam can be seen to be formed in the photo on the right. Operating the source using N_2 showed distinct differences from Ar operation. For example, higher flow rates ($\sim$40 sccm) and lower magnetic field intensities (below 1200 G) were required for best antenna-to-plasma coupling and discharge stabilization. Under these conditions, a full 1.2 kW of RF power was able to be delivered to the antenna.

Plasma source operation was also attempted with air, an N_2/Ar mixture, and xenon (Xe). A stable discharge was achieved in each case. Running the experiment during a continuous transition from pure N_2 to pure Ar with fixed magnetic field intensity and sporadic tuning of the RF impedance-matching circuit demonstrated the ability to deliver $\sim$800 W for any N_2/Ar proportion [11, 13]. An example of operation using the mixture of the gases is presented in figure 2-5. The photograph

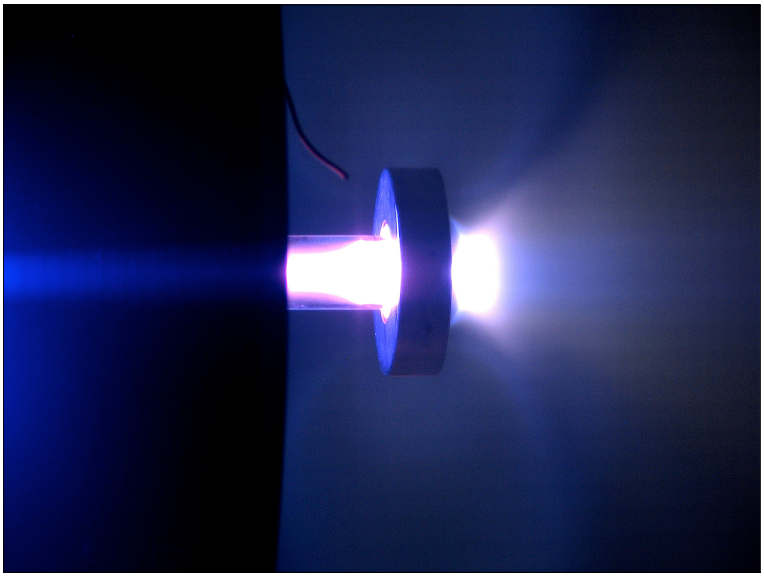

Figure 2-6: Operation at 20 sccm Ar gas flow with a permanent ceramic magnet in view at the end of the source tube. Note the constriction of the plasma column followed by an abrupt expansion to what appears to be a planar structure in the upstream region. Also note the semi-spherical structure in the downstream, plume region.

on the right shows the operation of the system with air taken directly from the lab atmosphere.

As a part of initial testing, permanent Neodymium and ceramic magnets have been used in addition to the aforementioned electromagnets [11]. A stable helicon discharge was obtained in all of these cases, as well. For a certain configuration, double-layer-like structures have been observed in the flow as shown in figure 2-6. An attempt is being made to characterize this observation more deeply using lab diagnostics and adaptive kinetic modeling [14, 23, 24, 25, 26, 27].

Chapter 3

Plume Diagnostics

There are a variety of diagnostic techniques for characterizing a plasma depending on the target parameter to be studied. These techniques can be separated into two main categories: intrusive and non-intrusive. An intrusive technique is characterized as one in which a physical probe is placed in the plasma and, thus, perturbs the plasma. This perturbation can be minimal or significant depending on the dimensions of the probe as compared to the characteristic dimension of the plasma. As a result, there are situations in which intrusive diagnostics fall second to non-intrusive methods. Non-intrusive methods include a variety of optical techniques such as emission spectroscopy and microwave interferometry; however, these techniques typically suffer from the need for a sizable financial investment and a rather complex experimental setup. Typical intrusive techniques include Langmuir probes, Faraday probes, and Retarding Potential Analyzers (RPA). These probes are usually simple in construction and, as such, are rather economical. While both categories can accomplish similar goals, the scope and budget of this research specified the use of intrusive diagnostics in order to diagnose the plume region of the helicon plasma source.

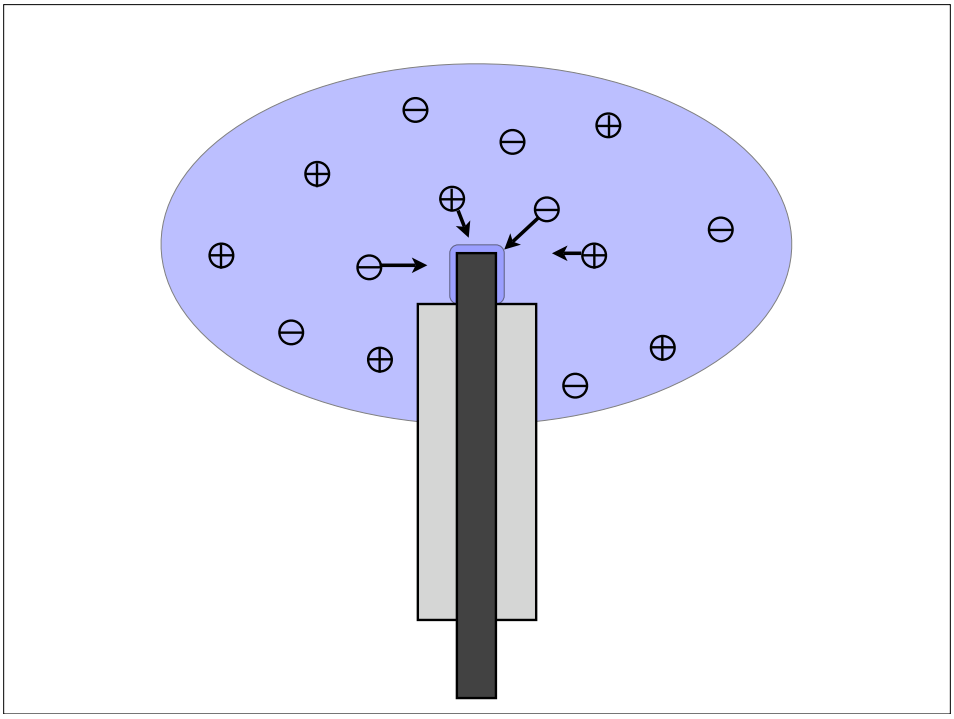

Figure 3-1: A pictorial representation of a Langmuir probe immersed in a plasma. Notice the small metal tip and the sheath surrounding it.

3.1 The Langmuir Probe

The Langmuir probe is the simplest of the intrusive instruments. In its most basic form, it consists of a rod of tungsten, which serves as a single electrode. The rod is typically insulated with a sheath of ceramic material along its entire length save a small tip that is left exposed. In practice, any refractory metal can be used; however, tungsten seems to be the most popular due to its relatively low cost and high availability. The rod itself may range in size from sub-millimeter to several millimeters in diameter, although, the perturbation caused by the probe is proportional to the characteristic dimension of the probe tip as compared to the characteristic dimension of the plasma to be diagnosed, so its diameter is a practical consideration to be made by the experimentalist. See Figure 3-1 for a simple representation of a Langmuir

probe.

The Langmuir probe can be used to determine the plasma and floating potential and the electron temperature and density by way of sweeping the potential applied to the electrode over a range of negative and positive voltages while immersed in the plasma. While doing so, an instantaneous current is measured corresponding to the instantaneous applied potential and a current-voltage (I-V) characteristic curve is constructed. From this I-V curve, the plasma parameters can be determined with appropriate application of the Langmuir probe theory.

3.1.1 The Electrostatic Sheath

The classical Langmuir probe theory is based upon the concept of the plasma or electrostatic sheath, which is a structure formed on any solid surface in contact with a plasma. The existence of the sheath arises as a result of the disparity in electron and ion fluxes to the collecting surface. The pre-sheath and sheath fluxes are a function of the electron and ion densities as well as the temperatures and masses of the particles and can be expressed as follows:

Pre-sheath:

$$\begin{aligned} \Gamma_e &= n_e \sqrt{\frac{kT_e}{2\pi m_e}} \\ \Gamma_i &= n_i \sqrt{\frac{k\left(T_e + ZT_i\right)}{m_i}} \end{aligned} \tag{3.1.1}$$

Sheath:

$$\begin{aligned} \Gamma_e &= n_e \sqrt{\frac{kT_e}{2\pi m_e}} e^{-\frac{e\Delta\phi_s}{kT_e}} \\ \Gamma_i &= n_i \sqrt{\frac{k\left(T_e + ZT_i\right)}{m_i}} e^{-\frac{1}{2}} \end{aligned} \tag{3.1.2}$$

Where n_e and n_i are the electron and ion densities, respectively and are assumed to be approximately equal due to the assumption of quasi-neutrality, k is Boltzmann's constant, T_e, T_i, m_e, m_i are the electron and ion temperatures and masses, respectively, Z is the charge state of the ion species, and $\Delta\phi_s$ is the sheath potential [2].

Now, since the plasma is assumed to be quasi-neutral, the densities will be unified and expressed as $n_e \approx n_i = n$. Also, most laboratory plasmas are considered to have cold ions, which means that the ion temperature is significantly lower than the electron temperature so as to be able to safely neglect that term in the above equations. That is, $T_e \gg T_i$. Applying these changes to equations (3.1.1), and taking the ratio of electron to ion fluxes in the pre-sheath, it is found that

$$\frac{\Gamma_e}{\Gamma_i} \approx \sqrt{\frac{m_i}{2\pi m_e}} \tag{3.1.3}$$

This value can be many times greater than unity and, in fact, in the case of Argon ($m_i = 39.95 m_{proton}$) as the working fluid, it is approximately 108. Because of the fact that electrons stream to the surface in contact with the plasma at a rate much greater than that of the ions, the surface accumulates a net negative charge. The accumulation of this negative charge value grows until a balance between electron and ion fluxes is met, thus creating a "potential sheath." That is to say that the electron flux is retarded and the ion flux is accelerated by negative surface potential until an exact equilibrium is reach and there is no net charge exchanged across the boundary of the sheath. The potential at which the sheath is located is referred to as the floating potential and can be found by equating equations (3.1.2) and solving for $\Delta\phi_s$ as follows:

$$|\Delta\phi_s| = \frac{kT_e}{e} \ln \sqrt{\frac{m_i}{2\pi m_e}} \tag{3.1.4}$$

The exact location of the sheath boundary is a more complex topic and requires the satisfaction of what is referred to as the Bohm Sheath Criterion; however, for the purposes of this discussion, it is sufficient to mention that this is met when the ion

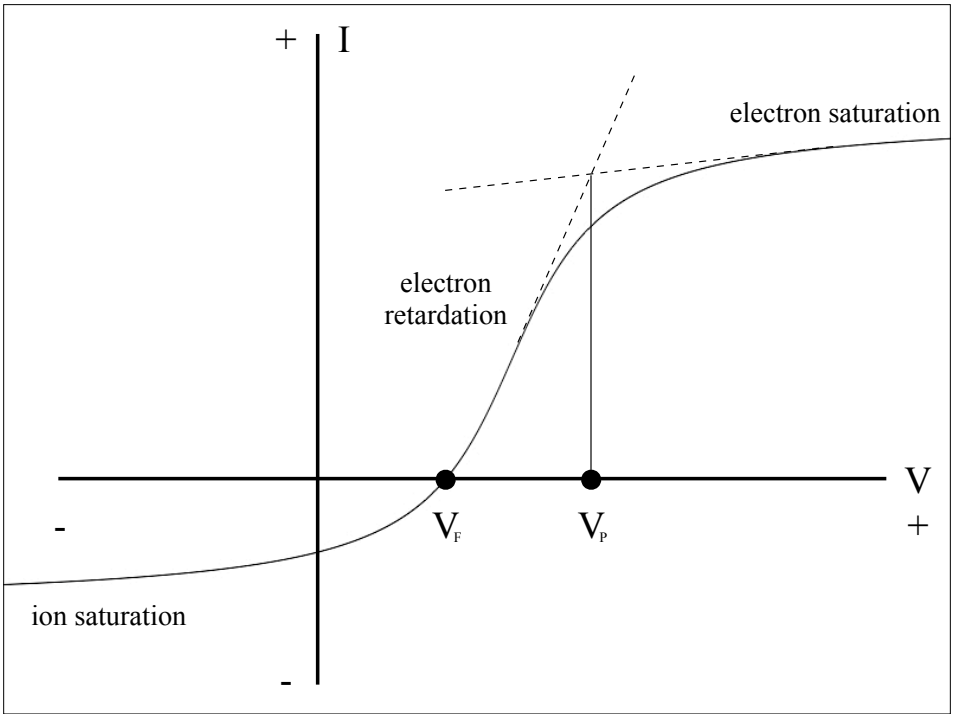

Figure 3-2: A plot showing the important aspects and regions of a typical Langmuir probe I-V curve. Notice that the floating potential is negative with respect to the plasma potential.

velocity becomes sonic:

$$u_i \geq c_s \approx \sqrt{\frac{kT_e}{m_i}} \tag{3.1.5}$$

Where u_i is the ion velocity and the same assumptions of cold ions has been applied to simplify the temperature term in the numerator. Also, the reader should note that, in the most strict sense, the Bohm Sheath Criterion is an inequality as shown in equation (3.1.5).

3.1.2 Langmuir Probe Theory

Now that a basis has been formed for an understanding of the electrostatic sheath, the specifics of its role in Langmuir probe theory can be discussed. There are a several regions of interest in a typical Langmuir probe I-V curve as shown in Figure 3-2. Referring to Figure 3-2 for the remainder of this discussion and going from left to right, the first region of interest is the ion saturation region. This is the region in which the probe has been biased sufficiently negative so as to repel all but the most high-energy electrons, thus preventing any greater negative charge build-up. This is characterized by a rapid leveling of the I-V curve to a negative current value [22, 34].

Following the ion saturation region is a brief but intense decrease in current. This occurs as a result of decreasing probe potential, thus permitting a increasingly greater number of electrons to reach the surface and culminates in a zero-current, potential value know as the floating potential, denoted as V_F. This is when the applied voltage on the probe produces an equilibrium in the electron and ion fluxes as discussed in the above section and is exactly synonymous with the equilibrium sheath potential case on a non-biased or floating-potential surface in the plasma.

The next region of interest is the electron retardation region. This lies between the floating potential and the plasma potential values and is characterized by a rapid increase in positive current due to the increasingly more positive probe bias. This causes a larger portion of the electron distribution to reach the probe surface and eventually leads to the electron saturation region. The plasma potential, V_P is the voltage value characterized by the rapid decrease in current from the electron retardation region to the electron saturation region. For voltages below V_P an electron sheath exists; however, when the probe bias potential is increased beyond V_P, the sheath shrinks until all electrons are permitted to reach the probe surface. This is now the electron saturation region and, of course, occurs as a result of a physical inability of a bulk of the ion distribution to reach the probe [22, 34].

3.1.3 Determination of Plasma Parameters

Floating and Plasma Potentials

With a basic understanding of Langmuir probe theory it is now possible to calculate the plasma parameters of interest from the information provided in the Langmuir probe I-V curve. First, the most simple values to determine are the floating and plasma potentials. The floating potential, V_F is simply the x-intercept value of probe potential. The plasma potential, V_P can be found by drawing tangents to the electron retardation and electron saturation regions and is the voltage value corresponding to the intersection point of the two tangents. The value can also be found more rigorously by taking the maximum of the first derivative of current with respect to voltage, namely $I'(V)$ [22, 34].

Electron Temperature

In order to determine the electron temperature, it must be assumed that the electron energy distribution function is purely Maxwellian. If this is the case, then the electron current in the retardation region can be written as an exponential function of the potential and temperature as follows:

$$I_e^r = en_eA_p\sqrt{\frac{kT_e}{2\pi m_e}}e^{\frac{eU}{kT_e}} \tag{3.1.6}$$

Where e is the fundamental charge, A_p represents the probe collection area, and $U = V - V_P$ has been introduced to denote the value of potential with respect to the plasma potential, the utility of which will become apparent in the electron density discussion. Now, upon taking the logarithm of equation (3.1.6) and differentiating with respect to potential, the final result is found to be

$$\frac{d\ln I_e^r}{dV} = \frac{e}{kT_e} \tag{3.1.7}$$

It should be noted that if the logarithm of equation (3.1.6), namely in the form

$\ln I_e^r = eV/kT_e + C$, is plotted on a log-linear scale, the relationship between $\ln I_e^r$ and V should be a linear one, whose slope is proportional to the electron temperature by equation (3.1.7); however, deviations from a linear relationship will indicate a non-Maxwellian electron energy distribution function [22].

Electron Density

To determine electron density, it is necessary to know electron temperature a priori using the above-mentioned method. Now, by taking equation (3.1.6) and considering the situation where $V = V_P$, it is found that $U = 0$ and the exponential term vanishes, leaving

$$I_e^r\left(V = V_P\right) = en_eA_p\sqrt{\frac{kT_e}{2\pi m_e}} \tag{3.1.8}$$

Further assumption that the characteristic dimension of the sheath is negligible compared to the dimensions of the actual probe tip itself allows the physically measurable area to be used for the probe area value. Of course an explicit equation for electron density only requires a trivial reorganization of equation (3.1.8).

3.2 Faraday Probe

The Faraday probe is a simple instrument that is used to measure the current density of the target plasma and ultimately, in combination with simultaneous electron density measurements from a Langmuir probe, can provide an estimate of the speed at which the bulk plasma is traveling. Another use is the opposite situation where the birth potential of the ions is known and hence, a value of ion velocity is able to be computed. In this case, the Faraday probe can then be used to determine electron density, which is often more accurate than Langmuir probe measurements.

The probe itself is not unlike a Langmuir probe in that it utilizes an electrode immersed in the target plasma; however, the main difference is that, rather than having a small tip, the Faraday probe has a plate-like electrode whose exposed area is

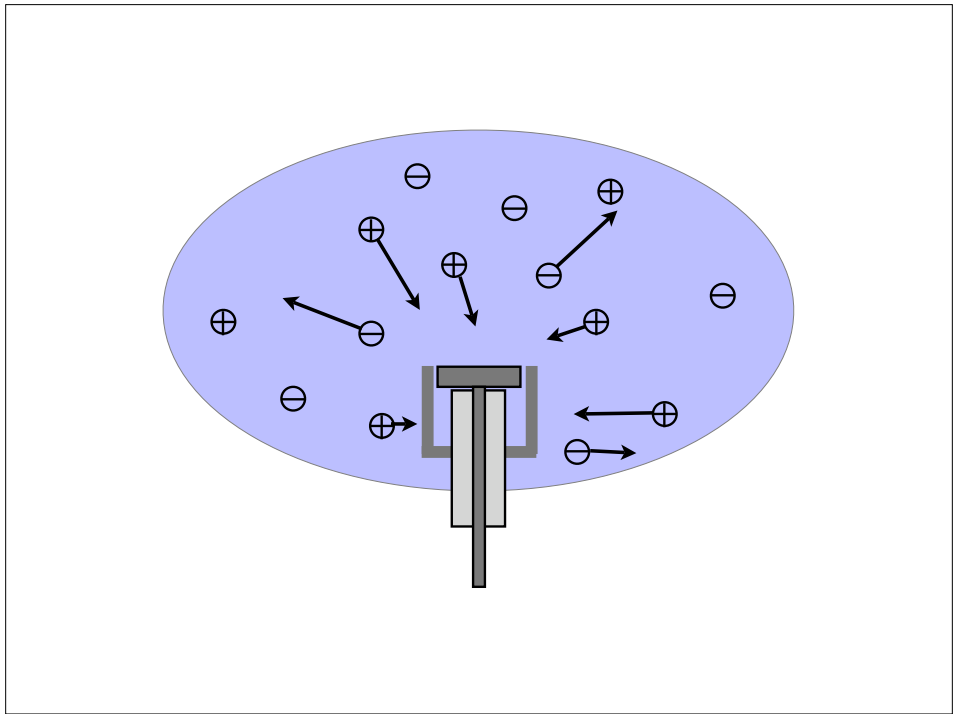

Figure 3-3: A pictorial representation of a Faraday probe in contact with the target plasma. Notice that the guard ring successfully attracts ions from the sides of the probe so as to collimate the field of view of the probe surface.

known precisely. Surrounding this flat-plate electrode is an electrically isolated ring known as a guard ring. In general operation, both the electrode and guard ring are independently biased at a sufficiently negative, but equal potential as to place the probe in the ion saturation region. In doing this, the guard ring collects a fair amount of current and "fools" the plasma, thus canceling geometrical fringe-field effects [34].

Figure 3-3 shows a diagram of a Faraday probe during operation. Notice that the guard ring is electrically isolated from the collector plate via the ceramic sheath surrounding the stem of the collector plate electrode; however, as mentioned above, it is not floating. Figure 3-4 shows the actual Faraday probe to be used. This particular design was originally developed by Azziz et. al. [34] at the MIT Space Propulsion Laboratory for use in Hall thruster plume diagnostics and has been reconstructed

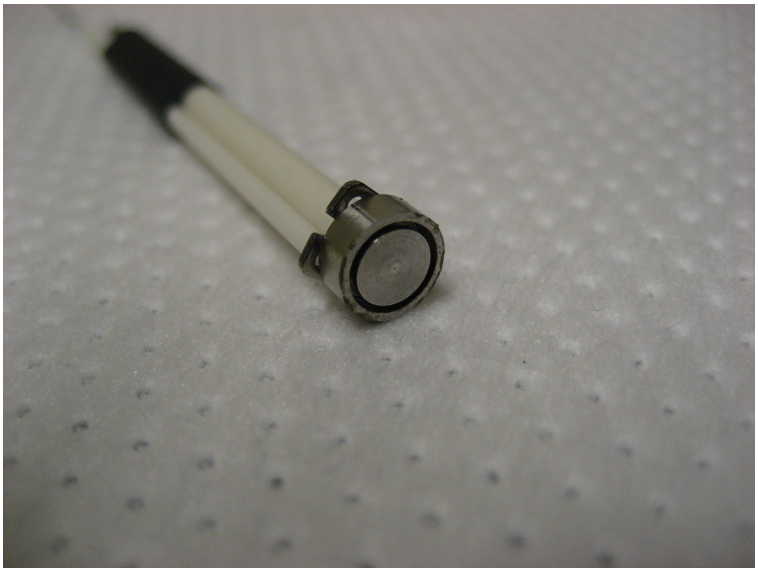

Figure 3-4: A photograph of the Faraday probe built for use in the mHTX@MIT program showing details of the guard ring, collector plate, and ceramic sheath.

and adapted for diagnosing the mHTX@MIT helicon plume. For practical purposes, both the guard ring and the collector plate should be biased at the same negative potential in the range of -8V to -20V, based on experiments performed by Azziz et. al. [34]. These voltages were found to place the probe well within the ion saturation region, while the fact that both were biased to the same potential produced a uniform sheath around both the collector plate and guard ring. For a fully detailed discussion of probe design considerations, the reader is referred to [34].

In practice, the Faraday probe measures a current that is induced by the ions incident on the collector plate. This current is then simply divided by the known area of the collector plate to determine the current density. The probe is typically swept in angle at some fixed radius from the plasma source exit to build a profile of current density as a function of angle. This, in turn, can be used to determine total plume current and plume divergence, which is a useful measure of the extent to which a plasma beam is collimated. Plume divergence is an important aspect of thruster performance when considering the possibility of plume impingement on nearby spacecraft surfaces and also specifies, to some extent, the proportion of the

ejected bulk plasma that is actually used to produce an on-axis thrust force. Equation (3.2.1) shows the relationship between current density, j, collected current, J_c, collector plate area, A_c, and ion velocity, v_i as follows:

$$j = \frac{J_c}{A_c} = en_e v_i \tag{3.2.1}$$

The plume can be considered a cone with a a spherical cap whose apex is centered at the origin of a spherical coordinate system (r, ϕ, θ), which is located at the center of the plasma source exit plane. The longitudinal axis of the plasma source is the z-axis and points in the positive direction. The location of the Faraday probe is then given by the radius, r specifying its distance from the origin and its angular location is fixed in zenith ($\theta = 0$) but is free to rotate in azimuth ($-\pi/2 \leq \phi \leq \pi/2$). Furthermore, it is assumed that the face of the Faraday probe is always facing the origin, that is to say that the longitudinal axis of the probe is collinear with a vector extending from the origin to the face of the Faraday probe with a magnitude of r and an azimuth of ϕ. Thus, the path of the Faraday probe describes the projection of a cone onto the x-z axis. In this system, assuming that the angular current distribution is axisymmetric, it is simple to see that to determine the total current contained in the plume, the following equation for the solid angle that is subtended by a half-cone of the type describe above is:

$$I_p = 2\pi r^2 \int_0^{\pi/2} j\left(\phi\right) \sin\left(\phi\right) d\phi \tag{3.2.2}$$

Equation (3.2.2) can then be augmented slightly in order to determine the plume divergence half angle by specifying a reasonable value of the beam current that should be contained within the plume and finding the half-angle at which this value is satisfied. In the past, researchers have used values in the range of 95 - 98% of the beam current. Based on the work of Azziz et. al. [34], the author suggests the use of 95% as a starting value. Equation (3.2.2) can be recast as a condition to be satisfied as follows:

$$0.95I_p = 2\pi r^2 \int_0^{\phi_{1/2}} j(\phi) \sin(\phi)\, d\phi \tag{3.2.3}$$

Finally, the most important calculation to be made for purposes of this work is that of the total plume energy or power. This can be done by way of capturing angular distributions of plasma potential and current simultaneously using a Langmuir probe and Faraday probe. The product of plasma potential and current at a given azimuth and radius is then the power and can be expressed as follows:

$$P(\phi) = J_c(\phi)\,(V_0 - V_P(\phi)) \tag{3.2.4}$$

Where V_0 is the ion birth potential and is determined from ion energy distribution data. The integral of equation (3.2.4) in the range $0 \leq \phi \leq \phi_{1/2}$ will then give the plume power

$$P_p = 2\pi r^2 \int_0^{\phi_{1/2}} P(\phi) \sin(\phi)\, d\phi \tag{3.2.5}$$

This result will then be used in the the global power balance model of the mHTX@MIT helicon source and will specify the value of the numerator in equation (5.3.3) for purposes of determination of the internal efficiency of the system.

3.3 Retarding Potential Analyzer

The final instrument to be discussed is what is typically referred to as a Retarding Potential Analyzer (RPA). The RPA is basically a collimated Faraday probe with the addition of a number of grids spanning the length of the instrument. Each grid is responsible for shielding the collector plate from a different class of particles by way of an applied potential. The first grid is typically left floating to shield the instrument from the bulk of the plasma. The second grid is referred to as the electron-repelling grid and is biased to a sufficiently negative voltage so as to repel electrons from further penetration into the probe body. The third and final grid is the ion-retarding grid

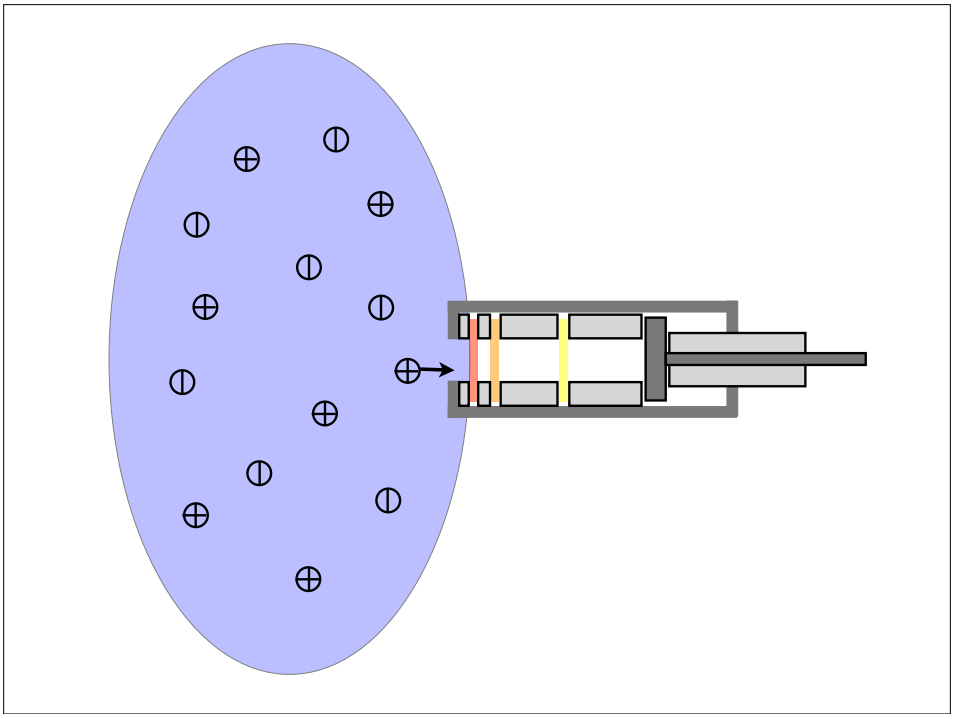

Figure 3-5: A pictorial representation of an RPA showing the three biased grids electrically isolated from each other by concentric, ceramic rings.

and is swept thru a range of voltages from zero to sometimes as high as 500V. As the potential of the ion-retarding grid increases, an increasingly greater number of ions are unable to travel up the potential to pass the grid and be collected. This effectively gives the experimentalist an I-V characteristic curve that describes the quantity of ions whose energies are those swept through by the RPA. This I-V curve is then used to determine the energy distribution of the ions in the target plasma, since the ion energy distribution is proportional to $I'(V)$.

It should be mentioned that in some RPA designs, a fourth grid is included just upstream of the collector plate. This is called the secondary-electron repelling grid and is positively-biased to prevent the measurement of an erroneously high current due to secondary-electron emission. Secondary-electron emission is caused by very

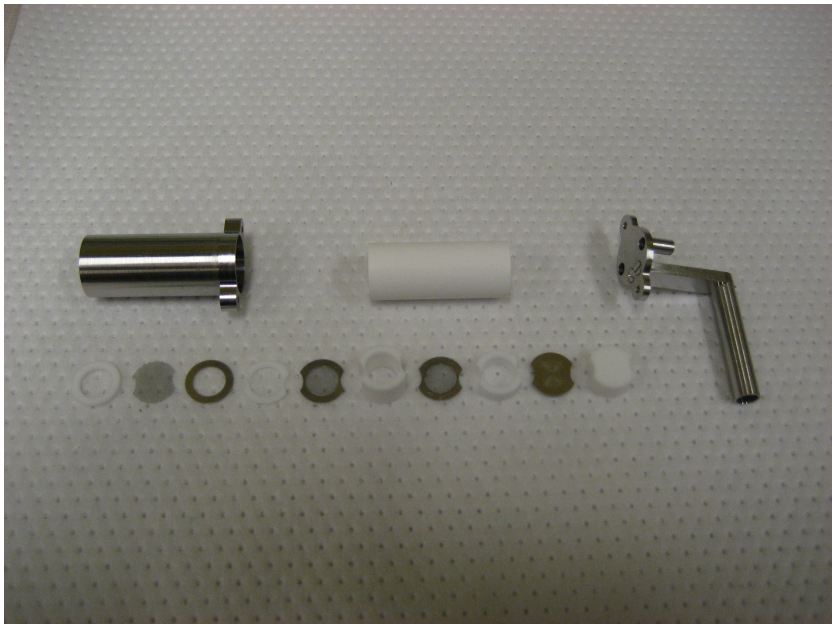

Figure 3-6: A deconstructed view of the mHTX@MIT RPA showing the individual grids, ceramic ring spacers, and the collector plate as well as the inner ceramic shell and the outer body.

high energy ions as they impact the collector-plate surface and can be dealt with by the addition of a fourth, positively-biased grid or by constructing the collector plate of a material with a higher work function, such as tungsten or another refractory metal. It should be noted; however, that at plume potentials lower than about 1 kV, this effect is small and can be corrected for from secondary-electron emission data [22, 34].

Figure 3-5 shows a picture of an RPA during operation. As with the Faraday probe, the particular RPA used for the mHTX@MIT diagnostics was developed by Azziz et. al. at the MIT Space Propulsion Laboratory. The original design has been reproduced for the purposes of this work and a photograph of the probe deconstructed to show the details of the grid arrangement is shown in Figure 3-6. Again, the reader is referred to [34] for details of the design of the RPA used in this work.

Chapter 4

Thermal Characterization

In order to determine the heat loading and associated losses to the source tube, it must be instrumented in such a way that the heat flux can either be directly measured or a suitable model can be applied to extract the heat flux from raw temperature data. There are a variety of methods that can be used to accomplish this goal; however, before choosing the most appropriate method, it is necessary to consider both the conditions and geometry in which these measurements are to be made, as well as the expectations placed on the results. In order to do this, it is important to understand the fundamentals of heat transfer so that the various methods can be evaluated objectively.

4.1 The Heat Equation

It is known from Fourier's law that heat flows in the direction opposite to a temperature gradient and as a result, the rate at which energy flows through a unit area, or the so-called heat flux is related to the temperature gradient as

$$q_x = -k\frac{dT}{dx} \tag{4.1.1}$$

Where, in this case, the x-directed heat flux, q_x is equal to the product of the derivative

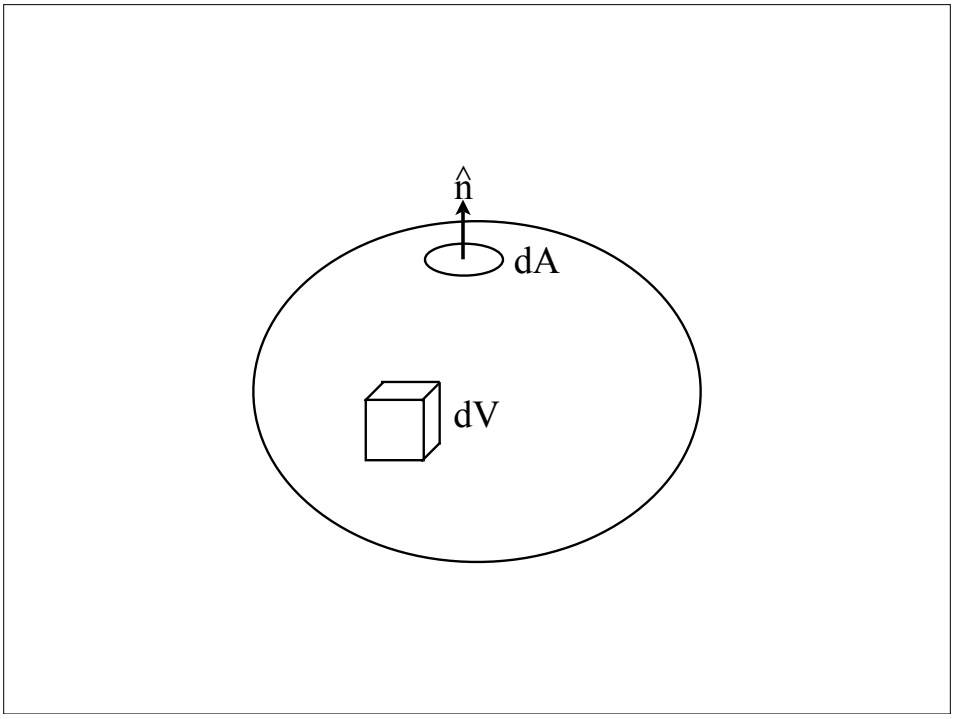

Figure 4-1: A pictorial representation of an isotropic solid with elemental volume dV and elemental area dA.

of temperature in the x direction and a proportionality constant, k, which is referred to as the thermal conductivity and has units of $Wm^{-1}K^{-1}$. The minus sign is used to indicate that energy flows from a high temperature to a low temperature. This can be readily extended to the more general, three-dimensional case as follows:

$$\mathbf{q} = -k\nabla T \tag{4.1.2}$$

Now consider the energy balance in a simple, isotropic solid as shown in figure 4-1, where the surface of the solid is defined by the normal vector $\hat{\mathbf{n}}$ and the solid is composed of small, elemental volumes, dV. In order to write an energy balance for this solid, the net rate of heat flow through the boundary of the solid and the time-rate of change of the internal energy must be equated to the rate of energy generation

in the solid. This can be written as follows:

$$\oint_A \mathbf{q} \cdot \hat{\mathbf{n}} \, dA + \int_V \rho C_v \frac{\partial T}{\partial t} \, dV = \int_V Q \, dV \tag{4.1.3}$$

Where ρ and C_v are the material density and constant-volume specific heat, respectively and Q represents the volumetric energy production rate in units of Wm^{-3}. Applying Gauss' theorem to the surface integral of the heat flux allows equation (4.1.3) to be recast as

$$\int_V \nabla \cdot \mathbf{q} \, dV + \int_V \rho C_v \frac{\partial T}{\partial t} \, dV = \int_V Q \, dV \tag{4.1.4}$$

Since this is a global energy balance, it also applies to any local volume within the solid and can therefore be rewritten as

$$\nabla \cdot \mathbf{q} + \rho C_v \frac{\partial T}{\partial t} = Q \tag{4.1.5}$$

Combining equation (4.1.5) with Fourier's law (equation (4.1.2)), the three dimensional heat equation with energy generation can be written as

$$-\nabla \left(k \nabla T \right) + \rho C_v \frac{\partial T}{\partial t} = Q \tag{4.1.6}$$

In general, the thermal conductivity, k of a material depends on temperature and so, in its current form, the heat equation is non-linear in temperature. If the assumption is made that the thermal conductivity is constant, then equation (4.1.6) can be recast as

$$\alpha \nabla^2 T + Q = \frac{\partial T}{\partial t} \tag{4.1.7}$$

Where $\alpha = k/\rho C_v$ is the thermal diffusivity of the material and is expressed in units of $m^2 s^{-1}$. Further assumptions can be made to reduce equation (4.1.7) to a more compact and readily solvable form. These will be discussed in greater detail in the following sections.

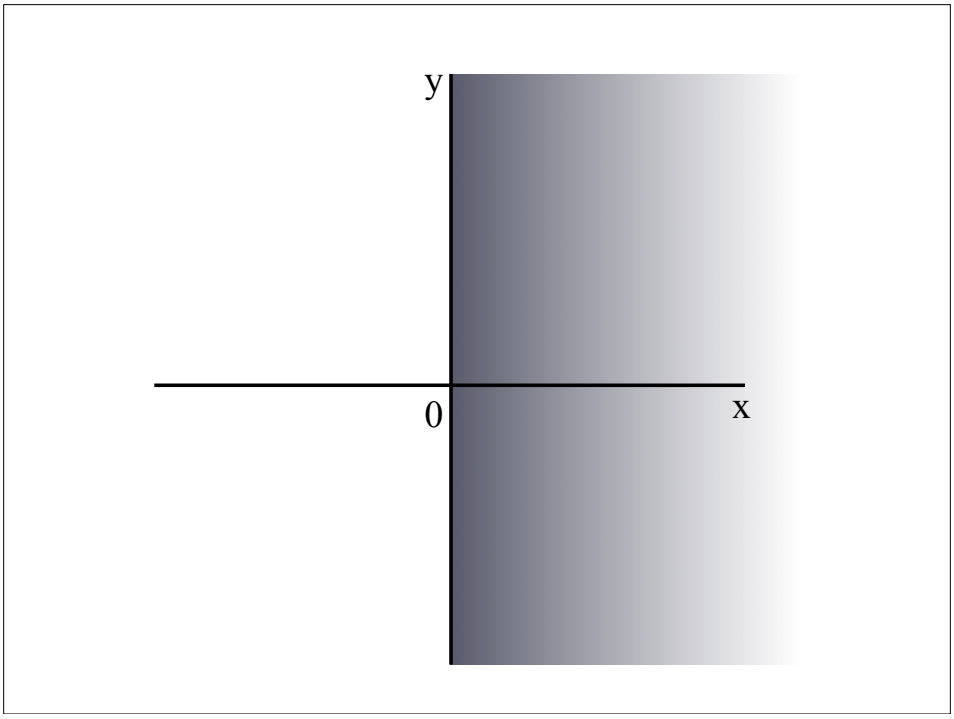

Figure 4-2: A pictorial representation of the half-space (semi-infinite) problem geometry.

4.1.1 The Half-Space or Semi-Infinite Problem

In order to provide some mathematical insight as to the nature of physical systems governed by the heat equation, a simple solid without internal energy generation will now be examined. Figure 4-2 shows a solid material in the x-y plane with a boundary located at $x = 0$ and extending to infinity in the positive and negative y directions and positive x direction. As a result of such geometry, this is commonly referred to as the half-space or semi-infinite problem [28, 30]. The initial temperature of the solid is assumed to be $T = T_i$ in the domain $0 < x < \infty$ and the temperature at $x = \infty$ is

$T = T_i$ for $0 < t < \infty$. This problem can be formulated as follows:

$$\begin{aligned} \alpha \frac{\partial^2 T(x,t)}{\partial x^2} &= \frac{\partial T(x,t)}{\partial t} \\ T(x,0) &= T_i \\ T(\infty,t) &= T_i \end{aligned} \tag{4.1.8}$$

Equation (4.1.8) is a linear, second-order, partial differential equation; however, by employing the Laplace transform, it can be reduced to a second order ordinary differential equation whose solution is easily acquired. Recall that the Laplace transform is defined as

$$\mathscr{L}[T(x,t)] = \bar{T}(x,s) = \int_0^\infty T(x,t)\, e^{-st}\, dt \tag{4.1.9}$$

Transforming equation (4.1.8) and its initial and boundary conditions gives

$$\begin{aligned} \frac{d^2 \bar{T}(x,s)}{dx^2} &= \frac{1}{\alpha}\left[s\bar{T}(x,s) - T(x,0)\right] \\ \bar{T}(x,0) &= \frac{T_i}{s} \\ \bar{T}(\infty,s) &= \frac{T_i}{s} \end{aligned} \tag{4.1.10}$$

Equation (4.1.10) is now solvable by assuming a general solution of the form

$$\bar{T}(x,s) = Ae^{-\sqrt{\frac{s}{\alpha}}x} + Be^{\sqrt{\frac{s}{\alpha}}x} + \frac{T_i}{s} \tag{4.1.11}$$

By considering the boundary condition $\bar{T}(\infty,s) = T_i/s$, it is readily apparent that as $x \to \infty$, the solution $\bar{T}(x,s) \to T_i/s$, thus the coefficient B must be equal to zero. This gives

$$\bar{T}(x,s) = Ae^{-\sqrt{\frac{s}{\alpha}}x} + \frac{T_i}{s} \tag{4.1.12}$$

Where the coefficient A will be determined by the boundary condition to be specified at $x = 0$.

Constant Surface Temperature Case

Consider the half-space problem described above by equation (4.1.8); however, let the boundary condition at $x = 0$ and its associated Laplace transform be specified as

$$\begin{aligned} T(0,t) &= T_s \\ \bar{T}(0,s) &= \frac{T_s}{s} \end{aligned} \tag{4.1.13}$$

This represents the instantaneous application of a constant surface temperature to the boundary of the semi-infinite solid. Applying the boundary condition in equation (4.1.13) to equation (4.1.12), the following solution is found

$$\bar{T}(x,s) = \frac{T_s - T_i}{s} e^{-\sqrt{\frac{s}{\alpha}}x} + \frac{T_i}{s} \tag{4.1.14}$$

Finally, using the inverse Laplace transform and rearranging, the solution can be expressed as

$$\frac{T(x,t) - T_i}{T_s - T_i} = erfc\left(\frac{x}{\sqrt{4\alpha t}}\right) \tag{4.1.15}$$

Where $erfc(x) = 1 - erf(x)$ is the complementary error function. This solution can be found in a variety of Laplace transform tables.

Now, by considering the units of the arguement of the complementary error function in equation (4.1.15), it can be readily seen that it is a non-dimensional group in length, which will, henceforth, be referred to as the non-dimensional thickness. Also, the left-hand side is a non-dimensional group in temperature. Then equation (4.1.15) can be rewritten by introducing non-dimensional variables as follows:

$$\Theta = erfc\ \chi \tag{4.1.16}$$

The non-dimensional temperature is plotted versus the non-dimensional thickness from Equation (4.1.15) in figure 4-3. Notice that the magnitude of Θ is negligible beyond $\chi = 2$. This result is significant in that it formally defines the concept of

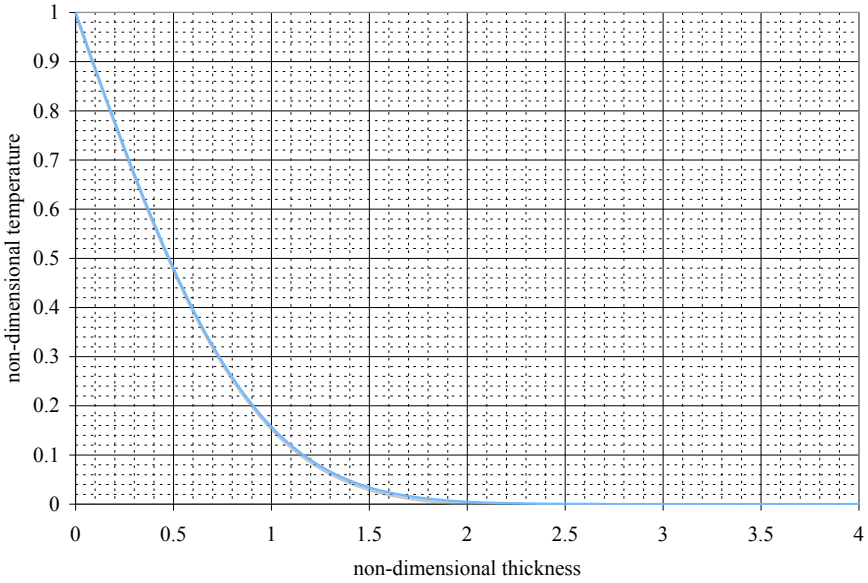

Figure 4-3: Notice that the non-dimensional temperature is negligible beyond non-dimensional thickness of 2. This region is referred to as the thermal boundary layer.

a semi-infinite material. From this, it can be stated that any medium whose non-dimensional thickness is greater than $\chi = 2$, can be referred to as a semi-infinite medium. That is, in the time range of interest, its characteristic dimension associated with heat transfer is sufficiently large compared to the distance to which the temperature disturbance propagates, so as to negate the effects of the disturbance beyond that distance. The zone of material contained in the range $0 < \chi < 2$ can also referred to as the thermal boundary layer [28, 30].

This is a useful concept, because it allows the researcher to determine, for a given measurement time, the minimum thickness required of the material of interest in order to be treated as semi-infinite for purposes of data interpretation. This thickness is

clearly given by

$$\delta = 4\sqrt{\alpha t} \tag{4.1.17}$$

However, the complementary question might be of greater utility: Namely, given a material whose thickness is known or set a priori, what is the maximum measurement time allowed in order to still consider the solid as semi-infinite? Rearranging equation (4.1.17), this characteristic time can be written as

$$\tau = \frac{x^2}{16\alpha} \tag{4.1.18}$$

Both equations (4.1.17) and (4.1.18) can be treated as guidelines for the use of the semi-infinite assumption when temperature is to be measured experimentally.

Constant Surface Heat Flux Case

The case of constant surface heat flux incident on the left boundary of a semi-infinite solid will now be considered briefly. The formulation of this problem takes the same form as in equation (4.1.8); however, the boundary condition on T is replaced with a condition on the derivative of T:

$$\begin{aligned} -k\frac{\partial T}{\partial x}\Big|_{x=0} &= q_s \\ \frac{\partial \bar{T}}{\partial x}\Big|_{x=0} &= -\frac{q_s}{ks} \end{aligned} \tag{4.1.19}$$

Combining this boundary condition with equation (4.1.12) gives the solution in the s-domain as

$$\bar{T}(x,s) = \frac{q_s}{ks}\sqrt{\frac{\alpha}{s}}e^{-\sqrt{\frac{s}{\alpha}}x} + \frac{T_i}{s} \tag{4.1.20}$$

As with the constant surface temperature case, the inverse transform of equation (4.1.20) can be readily found in a table of Laplace transforms to be

$$T(x,t) = T_i + \frac{q_s}{k}\left[2\sqrt{\frac{\alpha t}{\pi}}e^{-\frac{x^2}{4\alpha t}} - x\ erfc\left(\frac{x}{\sqrt{4\alpha t}}\right)\right] \tag{4.1.21}$$

Which, in non-dimensional form becomes

$$\Theta = \frac{(T(x,t) - T_i)\, k}{q_s \sqrt{\alpha t}} = \frac{2}{\sqrt{\pi}} e^{-\chi^2} - 2\chi \; erfc \; \chi \tag{4.1.22}$$

Note that the non-dimensional thickness is again present in the solution. By considering the solution at $x = 0$, physical insight can be gained with regard to the manifestation of a constant surface heat flux in experimental temperature measurements. By setting $x = 0$, equation (4.1.21) is reduced to

$$T(0,t) = T_i + \frac{2q_s}{k}\sqrt{\frac{\alpha t}{\pi}} \tag{4.1.23}$$

This indicates that temperature rise at the surface $x = 0$ is proportional to the square root of time, which provides the researcher with a heuristic for real-time, qualitative estimation of surface heat flux conditions in the field.

4.2 Measurement of Heat Flux

As was mentioned at the beginning of this chapter, there are many ways in which heat flux is typically measured experimentally. Usually, these methods employ either thermocouples, resistance thermometers, or other means of direct temperature measurement, or a heat flux sensor [29, 30]. It is necessary to note that all methods are similar in their need for application of the appropriate physical model of the sensor and system in order for a meaningful interpretation of the data to be made. This section will draw upon the developments of the previous section in an attempt to develop a first-order method for determination of heat flux to and power gained by the source tube.

4.2.1 The Inverse Heat Conduction Problem

In many engineering systems, it is necessary to determine the heat flux incident upon a given surface for purposes of diagnosing or controlling a given process. This can be a straightforward problem to solve in a situation where the surface of interest is easily accessible. In such a case, thermocouples or heat flux sensors can be applied to the surface and heat flux can be deduced using an appropriate direct analytical method [29]. However, there are situations in which the surface of interest is either not accessible due to apparatus geometry or is exposed to conditions that would endanger the sensor. Such problems are known as inverse heat conduction problems (IHCP) and happen to be quite a bit more complicated than their direct or forward heat conduction problem counterparts.

The classical IHCP was first addressed by Stolz in 1960, who was interested in the experimental determination of heat fluxes involved in the quenching of simple shapes [30]. With the birth of the space age in the late 1950's and early 1960's, there was considerable effort given to the problem of determining heat fluxes to the surfaces of re-entry heat shields and rocket nose cones using indirect sensing methods. Also, internal combustion engines found their way into the world of IHCP's when it became of interest to determine heating rates in an engine's combustion chambers.

The IHCP is known to be a member of the class of mathematical problems termed ill-posed. This is to say that their solution does not satisfy the requirements of existence, uniqueness, and stability in the presence of small changes to the input data. The ill-posedness of the IHCP comes from the fact that the measured quantity, usually temperature, used to estimate the unknown quantity, namely heat flux, is not given at the same boundary as the heat flux itself [30].

Unlike the direct heat conduction problem where, given a known heat flux, the transient temperature history resulting from that heat flux is determined, the IHCP seeks to determine the heat flux responsible for producing the measured transient temperature history. In essence, the IHCP can simply be describe as a method to determine the cause through use of information regarding the effects. Application of

the IHCP is not limited to heat flux determination, but can be used in the determination of various thermal properties such as thermal conductivity or heat transfer coefficients as well.

Unfortunately, the IHCP method is still quite an active topic of research in regard to both the appropriate application of the diagnostics tools and also the mathematics required to correctly analyze and interpret the resulting data. The author originally intended to employ this method to determine the incident heat flux on the inner wall of the source tube; however, through subsequent studies, it has been determined that the effort required to construct, test, and validate a full IHCP model of the mHTX system is well beyond the scope of this work. The reader is referred to [31, 32] for further reading on various topics still being actively researched in the IHCP field.

4.2.2 Calorimetry

Calorimetry is the method of determination of energy transport indirectly by way of the measurement of temperature changes in the object of interest. Historically, this method is deeply rooted in the foundation of thermochemistry and was first employed by Antoine Lavoisier and Pierre-Simon Laplace, to determine the evolution of heat as a result of various chemical reactions [30]. In fact, this method can be developed directly from the First Law of Thermodynamics, which is generally a statement of conservation of energy. The First Law of Thermodynamics states very specifically that the increase in internal energy of a system is the difference between the heat energy added to the system and the work done by the system on its surroundings. In mathematical terms, this can be written as

$$dU = \delta Q - \delta W \tag{4.2.1}$$

Where dU represents the increment in internal energy of the system, δQ represents the energy added to the system without specification of the process by which this energy is added, and δW represents the work energy lost by the system's work done

on its surroundings. For purposes of this work, the quartz plasma source tube will be considered the system. Throughout all experiments, this tube will remain at constant pressure and volume and so, for purposes of simplification, equation (4.2.1) can be reduced to

$$dU = dQ \tag{4.2.2}$$

This is due to the fact that the work term in equation (4.2.1) refers specifically to work done by changes in pressure or volume and can be equivalently expressed as $\delta W = PdV$, where P represents the system pressure and dV represents a change in system volume. From equation (4.2.2), it is easy to develop the simple calorimetry equation to be used for determination of heat evolution. Experimentally, a change in system temperature will be measured, which, upon combination with the appropriate physical constants, will provide a measurement of the change in internal energy and, thus, the change in heat or energy of the system. Thus, the final calorimetry equation to be used is

$$\Delta Q = mc_p\Delta T \tag{4.2.3}$$

Where ΔQ is the heat added to the system, which will result in a change in its internal energy, m is the mass of the system, c_p is the specific heat capacity of the material comprising the system, and ΔT is the change in temperature of the system. Note first, that the right-hand side of equation (4.2.3) actually represents the internal energy from equation (4.2.2). Also, the reader should be aware that, in general, the heat capacity of a substance takes different forms depending on the nature of the process in which the system is involved. Gases and liquids have different heat capacities, namely one for a constant-pressure process, C_p and one for a constant-volume process, C_v, which are both extensive properties. In solids, both pressure and volume do not vary and, as such, both values are the same. The use of specific heat as an intensive property in equation (4.2.3) allows the experimentalist the ability to

Property	Value
density (kg/m^3)	2200
thermal conductivity (W/mK)	1.38
specific heat (J/kgK)	740
thermal diffusivity (m^2/s)	8.48×10^{-7}

Table 4.1: Typical properties of fused quartz.

specify the mass of the system being diagnosed.

To make equation (4.2.3) consistent with the global power balance being constructed, it can simply be recast as follows:

$$P_i = \frac{\Delta Q}{\Delta t} = mc_p \frac{\Delta T}{\Delta t} = mc_p \frac{T_i - T_{i-1}}{t_i - t_{i-1}} \tag{4.2.4}$$

Where P_i represents the instantaneous power gain of the source tube and Δt is the increment in time between temperature measurements. Equation (4.2.4) allows the experimentalist to determine the rate at which energy is entering or leaving the system by way of transient temperature measurements. All that is needed is knowledge of the material properties of the system and an instrument to measure the transient temperature profile of the system. Furthermore, the average power gained, which should agree well with the actual heat flux incident on the system when considering the incident area, can be computed from the temperature data and using equation (4.2.4) as

$$P_{avg} = \frac{\sum_{i=0}^{N} P_i}{\sum_{i=0}^{N} i} \tag{4.2.5}$$

Example: Simulated Heat Flux

This section briefly covers an analytical example of the above method to show its consistency. The system to be considered is a constant-cross-section quartz tube

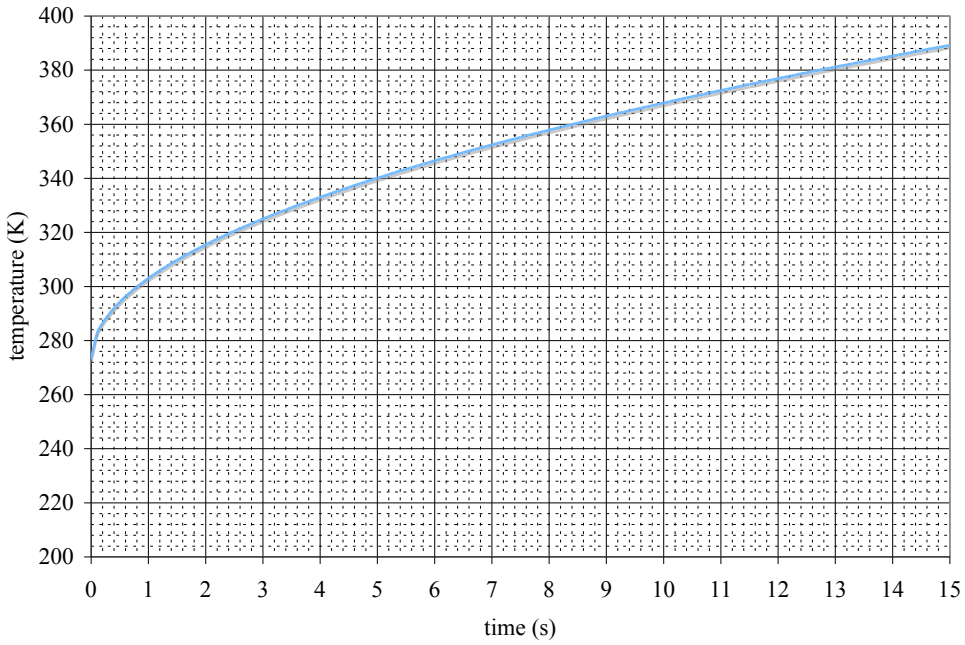

Figure 4-4: A plot of the simulated temperature profile on the quartz tube using equation (4.1.23) as discussed in the given example.

having an inner and outer diameter of 2 cm and 2.3 cm, respectively, a length of 40 cm and having a mass of 0.16 kg. Its inner surface is exposed to a 1000-W power source with a corresponding, uniform heat flux of 39.7 kWm^{-2}. Table 4.1 [33] lists typical values for quantities of interest to this work. Considering a wall thickness of 1.5 mm and using the values listed in table 4.1 in concert with equation (4.1.18), the characteristic time for thermal equilibration across the wall is found to be approximately 0.17 s. As a result, using a simulated measurement time of 15 s should sufficiently justify the assumption that the system is thermally thin. This is to say, that for purposes of temperature measurement, it can be asssumed that the thermocouple will measure the same temperature on the outer wall as is present

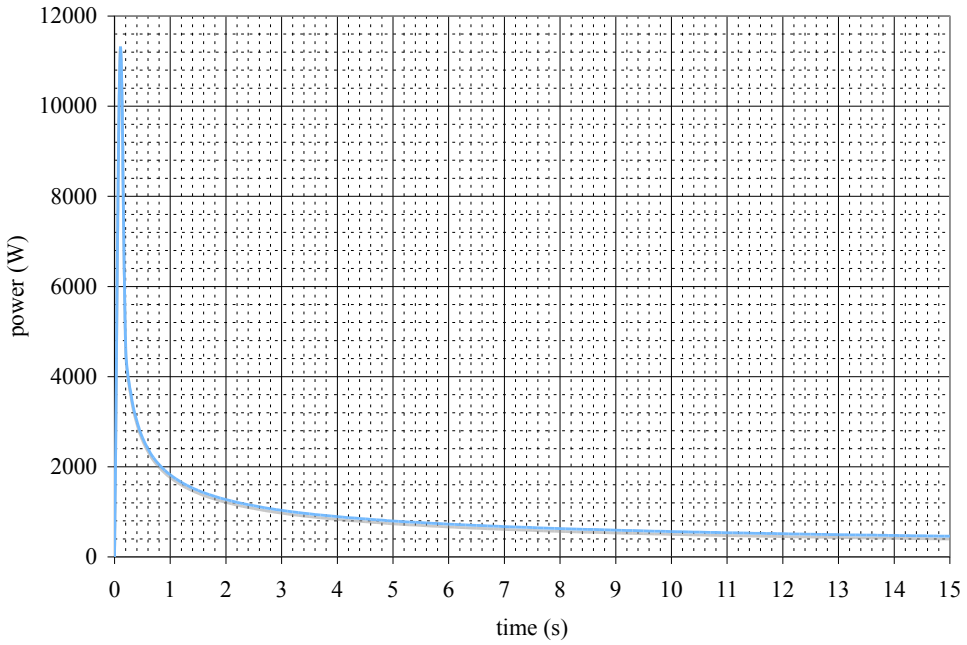

Figure 4-5: A plot of the resultant power data reduced from the temperature series in Figure 4-4 using equation (4.2.4).

on the inner wall. Furthermore, the tube is assumed to be instrumented with a thermocouple whose junction characteristic dimension is on the order of 0.1 mm and is placed on the outer surface of the tube. Finally, the ratio of wall radius of curvature to junction dimension is found to be approximately 100, which is sufficient to justify the assumption of a flat plate model.

Using equation (4.1.23), a simulated temperature profile can be built based on the assumption of a constant surface heat flux. Applying equations (4.2.4) and (4.2.5) to the resulting data series, values for the instantaneous and average power absorbed by the quartz tube can be computed. Using a simple spreadsheet model, the following two plots given in Figures 4-4 and 4-5 were created as described above. Using equation

(4.2.5), the average power gain of the quartz tube was found to be $P_{avg} = 910.9\ W$ corresponding to a surface heat flux of $q_s = 36.2\ kWm^{-2}$, resulting in an error of 8.9% from the input quantities of $P = 1000\ W$ and $q_s = 39.7\ kWm^{-2}$. Though this could be considered to be a moderate error, the reader must be reminded that this study is an introductory one and more detailed methods should be sought out and examined before rendering a final judgement as to the best method by which to evaluate power gain by the source tube. Furthermore, the author asserts that errors on the order of 10 % or lower are within acceptable limits for a first attempt at a global mapping of energy transport in a helicon plasma source.

Chapter 5

Energy Balance Model

This chapter covers the construction of a global energy balance model of the mHTX@MIT helicon plasma source. This model draws upon the discussions in Chapters 3 and 4 in its development and covers the entire system from the radio frequency (RF) power supply to the plasma plume with a discussion of the appropriate assumptions, considerations, and exclusions made. The result is a complete model that should be able to give the experimentalist valuable information regarding losses incurred via radiation and poor magnetic confinement to the source tube, the proportion of useful "losses" to the plume, an approximate antenna-plasma coupling efficiency, and finally an approximate internal efficiency for the system as a whole. From this point forward, the author will refer to power as the quantity of interest rather than energy, though the reader should be reminded that the character of the analysis is not changed by this nomenclature and this still remains, in either form, a balance of energy or energy per unit time of the helicon system.

5.1 Power System

For the purposes of this work, the power system will be considered to encompass all components between the Advanced Energy RFPP-10 1.2 kW RF power supply and the helicon antenna. This includes a 5-m section of RG-214 coaxial cable connecting

the power supply to the impedance matching network, the network itself, the RF power feed through, and the coaxial transmission line connecting the vacuum-side of the power feed through to the antenna-plasma load. The reason for not considering each of the individual components of the power system is that there are various locations within the system that could potentially cause power reflections or absorptions other than the antenna-plasma load itself. A separate, very complex study could be performed on the losses incurred in the power system itself with no consideration made for the actual helicon plasma source.

The RF power supply is run via a LabVIEW program that allows the user to choose the power set point and in turn displays the forward, reflected and load power as a function of time. During any given test run, the load power may vary slightly or greatly depending on the nature of the impedance matching point being used for that test. As a result, tests should be short in duration so as to minimize large fluctuations in the antenna-plasma load power, lest these fluctuations be manifested in the data being taken.

5.2 Source Tube

The quartz tube shown as the top tube in figure 5-1 was constructed by QSI Quartz Scientific, Inc of GE grade 214 fused quartz whose physical properties are listed in table 4.1. The tube is 2 cm in inner diameter and 2.3 cm in outer diameter and has two main sections. The first and smaller of the two sections is comprised of a 2.3-cm section of 1/4-inch diameter quartz tube that is spun-welded to the main 2.3-cm diameter tube via a 2.5-cm long conical section of quartz. This serves a tube connector for the propellant feed line and accepts a standard 1/4-inch Swagelok Ultra-Torr fitting. The second section, of course, is the constant-cross-section main tube, which has a total length of 40 cm and ends in a flat, flame-polished exit plane.

As a component in the power balance model, there are two main assumptions that must be made. First, for purposes of temperature measurement, it will be

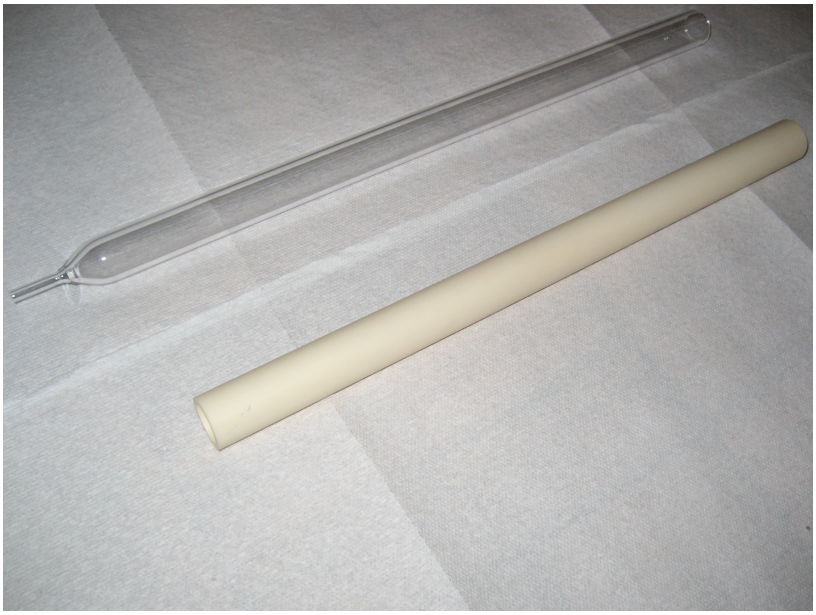

Figure 5-1: A photograph of the quartz source tube (top) and the alumina ceramic source tube (bottom).

assumed that the smaller conical-fitting section of the tube is neglected. This allows the experimentalist to assume longitudinal symmetry and simplifies reduction of the data. The second assumption to be made is that GE grade 214 fused quartz has a high degree of optical transmission ranging from approximately 160 nm to 4000 nm with only one small absorption in the 2730 nm water band, thus allowing for all but a small amount of radiation absorption to be ruled out in the temperature measurements. This ensures that a majority of the power gained by the tube is due to poor magnetic confinement.

5.2.1 Thermocouple Array

The source tube is instrumented with five, Omega Engineering, Inc C01-K type-K "Cement-On" surface-mountable thermocouples. A photograph of one of the thermocouples used can be seen in figure 5-2. Each thermocouple is bonded to the surface using Omega Engineering, Inc OmegaBond "200" High Temperature, High Thermal Conductivity Epoxy Adhesive to minimize thermal contact resistance, which would

skew measurement accuracy. The reader is referred to Appendix D for details of bonding the thermocouples to the tube. Each thermocouple is then connected to a type-K thermocouple extension wire via a mini-SMC connector and is run to one of five type-K adapters on the type-K 5-line thermocouple vacuum feedthrough attached to one of the Astrovac chamber's 2-3/4 inch Conflat ports.

Due to the length of the source tube and the potential variation in plasma properties over that length, one thermcouple will not suffice in the determination of power gained. So, to represent the source tube mathematically, it is discretized into five cylindrical cells as shown in figure 5-3. In order to capture the temperature variation at both end boundaries of the source tube, there are three inner cells whose lengths are 10 cm and have their respective thermocouples bonded to their central nodes and two boundary cells whose lengths are 5 cm that have thermocouples bonded to their edges. Each cell is considered to be separate from the others when performing calorimetric diagnostics. This is to say that the mass in equation (4.2.4) represents the mass of each cell, rather than that of the entire tube. Therefore, equations (4.2.4) and (4.2.5) can be recast as

$$P_{i,j} = m_j c_p \frac{T_{i,j} - T_{i-1,j}}{t_{i,j} - t_{i-1,j}} \tag{5.2.1}$$

$$P_{avg,j} = \frac{\sum_{i=0}^{N} P_{i,j}}{\sum_{i=0}^{N} i} \tag{5.2.2}$$

Where the subscript $_j$ represents the cell where the measurement was taken. Finally, to determine the total power absorbed by the source tube a simple sum of the cell-absorbed powers can be used as follows:

$$P_{tube} = \sum_{j=1}^{5} P_{avg,j} \tag{5.2.3}$$

Figure 5-2: A photograph of one of the C01-K surface thermocouples showing details of the junction.

Property	Value
density (kg/m^3)	3960
thermal conductivity (W/mK)	28
specific heat (J/kgK)	850
thermal diffusivity (m^2/s)	8.32×10^{-6}

Table 5.1: Typical properties of alumina ceramic.

Of course, it is assumed that all losses from the plasma occur axisymmetrically, thus allowing for such a simple, linear array of thermocouples and eliminating the need for an azimuthal array. For purposes of determining a rough estimate of power absorption profile over the tube length, a linear variation in absorbed power can be assumed between thermocouple nodes. This allows for a rough comparison of the absorbed power and axial magnetic field profile, which may provide insight as to the effects of the magnetic field intensity profile on tube losses.

Now, up until this point, only the confinement losses have been treated. In order to determine the radiation losses from the plasma, a different source tube is used.

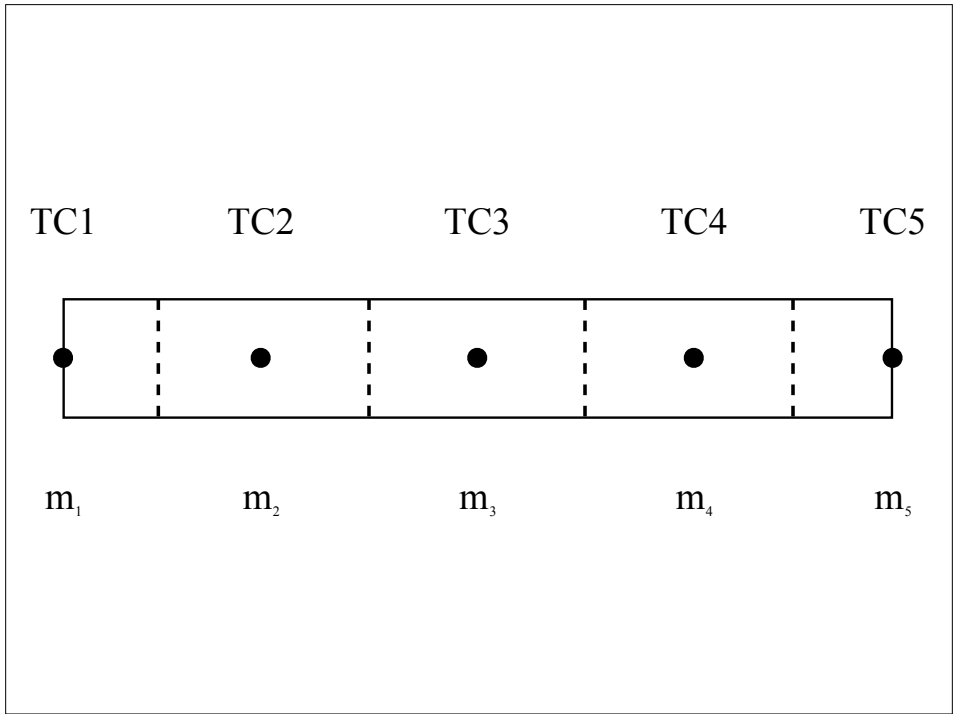

Figure 5-3: A pictorial representation of the source tube where the thermocouple nodes are numbered one through five and the masses $m_2 = m_3 = m_4 > m_1 = m_5$ refer to the masses corresponding to each of the five cells whose boundaries are given by the dotted lines.

This time, an alumina ceramic tube is used, whose properties are listed in table 5.1 and can be seen as the bottom tube in figure 5-1. The purpose for the use of this material is that it is opaque to all optical emissions and as such will absorb all radiation emitted from the plasma. This gives a value for power gained from radiation and confinement losses to compare to the quartz source tube value for power gained from mostly confinement losses. As a first approximation, it is sufficient to state that the difference between the two values is roughly equivalent to the radiation losses, given the same operation parameters for the helicon source.

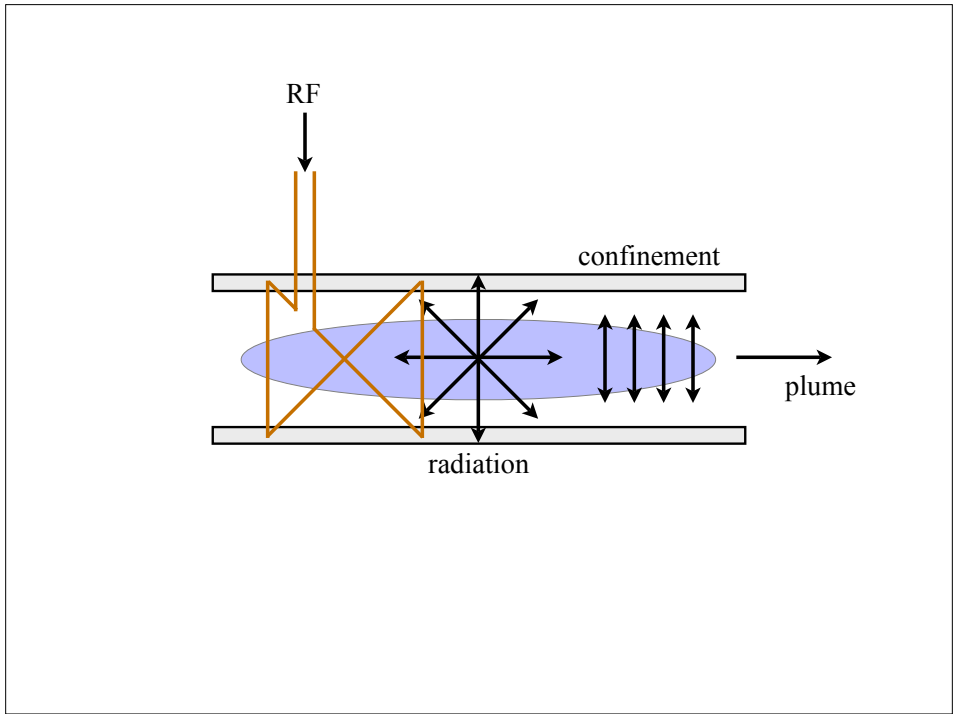

Figure 5-4: A pictorial representation of the mHTX@MIT helicon plasma source with all loss mechanisms considered.

5.3 System Efficiencies

Figure 5-4 shows a schematic of the complete energy balance model with each of the loss mechanisms identified. As was discussed in the above section, the source tube is instrumented in such away as to distinguish the proportion of power lost to plasma radiative processes and poor magnetic confinement. The plume energy is determined using the methods discussed in Chapter 3 and the RF power is known from the output given by the power supply. By combining all of the above developed concepts, a complete global energy balance is finally found to be

$$P_{RF} = P_{rad} + P_{con} + P_{plume} = P_{tube,Al} + P_{plume} \tag{5.3.1}$$

Where it can be seen that both radiation and confinement losses are able to be

lumped into one term, $P_{tube,Al}$ when measurements are done on the alumina ceramic source tube; however, the radiation power can be determined as a difference of the alumina ceramic and fused quartz tube powers, namely $P_{rad} = P_{tube,Al} - P_{tube,quartz}$. Furthermore, the power system-plasma coupling efficiency and the system internal efficiency are able to be computed as follows:

$$\eta_{RF} = \frac{P_{tube} + P_{plume}}{P_{RF}} \tag{5.3.2}$$

$$\eta_{I} = \frac{P_{plume}}{P_{RF}} \tag{5.3.3}$$

This completes the development of the simple energy balance model of the mHTX@MIT helicon plasma source and should provide for a good first-order approximation of losses and efficiencies incurred during the various stages of operation of the source.

Chapter 6

Conclusions

This thesis has discussed the details of helicon plasma sources in context to use in space propulsion. In particular, attention has been paid to the loss mechanisms incurred during regular helicon source operation. A discussion of the mHTX@MIT experimental facility was given to provide the reader with an appreciation for the program in terms of both past and future work. Both plume and source tube thermal diagnostics were discussed and methods were developed for determination of losses incurred in both these regions. This, of course, led to the construction of a simple energy balance model, which provides the reader with a first-order view of diagnosing power losses and various efficiencies in a helicon plasma source.

6.1 Recommendations for Future Work

In terms of future work, the author recommends that more detailed analyses of thermal characterization methods be performed in order that a more accurate and complete model be produced. As discussed briefly in Chapter 4, the Inverse Heat Conduction Problem methodology may prove to be very useful in accurately diagnosing not just losses to the source tube, but also in building a detailed heat flux topology that can be compared more easily to the magnetic field profile to determine the correlation between losses and magnetic field profile. This then leads to the recommendation that

a detailed mapping of the magnetic field topology be performed for various operating conditions so that such detailed thermal data could be compared to equally detailed field data.

Furthermore, it is suggested that, regardless of the future thermal model to be applied, more thermocouples be used to increase the resolution of the source tube temperature profile. This, of course, will require multiple thermocouple vacuum feed throughs or the use of a multi-channel thermocouple data logger that could be placed in the vacuum chamber during testing. This would allow the acquisition of the raw temperature data in the chamber to be converted from analog to digital values and then sent via a standard cable through a wire feed through and to the computer system for permanent logging.

Finally, the author wishes that, in the future of the mHTX@MIT program, a computational model be developed in an effort to complete the characterization of the mHTX@MIT helicon plasma source insomuch as it may be used to model experimental cases and perhaps shed more light on both the empirical observations made and the detailed, but rich and intriguing physical processes governing the helicon plasma source.

Appendix A

Helicon Cold Plasma Theory

A.1 Governing Equations

In order to arrive at the specific helicon dispersion relation, the general dispersion relation must first be derived. In the derivation that follows, a cold plasma composed of two particle species is assumed to be uniform and homogeneous in space and time and collisions are neglected. Furthermore, it is assumed that all wave amplitudes are sufficiently low to neglect second order terms, thus the linear wave approximation is valid, and all perturbed quantities are of the harmonic form $e^{i(\mathbf{k}\cdot\mathbf{r}-\omega t)}$, where $\mathbf{k}$ is the wave propagation vector and ω is the wave angular frequency. To begin, Faraday's Law and Ampere's Law will be considered as follows:

$$\nabla \times \mathbf{E} = -\frac{\partial \mathbf{B}}{\partial t} \tag{A.1.1}$$

$$\nabla \times \mathbf{B} = \mu_0 \left(\mathbf{j} + \epsilon_0 \frac{\partial \mathbf{E}}{\partial t} \right) \tag{A.1.2}$$

By applying the linear wave approximation to equations (A.1.1) and (A.1.2)

$$i\mathbf{k} \times \mathbf{E}_1 = i\omega \mathbf{B}_0 \tag{A.1.3}$$

$$i\mathbf{k} \times \mathbf{B}_0 = \mu_0 \mathbf{j}_1 - \frac{i\omega}{c^2} \mathbf{E}_1 \tag{A.1.4}$$

and combining them to eliminate $\mathbf{B}_0$ it is found that

$$\frac{i}{\omega}\mathbf{k}\times\mathbf{k}\times\mathbf{E}_1 = \mu_0\mathbf{j}_1 - \frac{i\omega}{c^2}\mathbf{E}_1$$

$$\mathbf{k}\times\mathbf{k}\times\mathbf{E}_1 + i\omega\mu_0\mathbf{j}_1 + \frac{\omega^2}{c^2}\mathbf{E}_1 = 0 \tag{A.1.5}$$

Where the subscript $_1$ indicates first-order quantities. Now, by using the general form of Ohm's Law $\mathbf{j} = \sigma\cdot\mathbf{E}$, equation (A.1.5) can be rewritten as

$$\mathbf{k}\times\mathbf{k}\times\mathbf{E}_1 + i\omega\mu_0\sigma\cdot\mathbf{E}_1 + \frac{\omega^2}{c^2}\mathbf{E}_1 = 0$$

$$-k^2\left(\mathbb{1} - \hat{\mathbf{k}}\hat{\mathbf{k}}\right)\cdot\mathbf{E}_1 + \frac{\omega^2}{c^2}\left(\mathbb{1} + \frac{ic^2\mu_0}{\omega}\sigma\right)\cdot\mathbf{E}_1 = 0$$

$$\left[-n^2\left(\mathbb{1} - \hat{\mathbf{k}}\hat{\mathbf{k}}\right) + \mathsf{K}\right]\cdot\mathbf{E}_1 = 0 \tag{A.1.6}$$

Where σ is the conductivity tensor, $\mathbb{1}$ is the unit tensor, $\hat{\mathbf{k}} = \mathbf{k}/k$ is a unit vector in the direction of the wave propagation vector, $n = kc/\omega$ is the index of refraction, $\mathsf{K} = \mathbb{1} + (i/\epsilon_0\omega)\sigma$ is defined as the dielectric tensor, and the tensor multiplying $\mathbf{E}_1$ is defined as the dispersion tensor, D. Equation (A.1.6) constitutes the most general form of the cold plasma dispersion relation; however, the dielectric tensor must be defined in more detail before going any further.

A.2 The Dielectric Tensor

Consider the linear equation of motion for a plasma of species s as follows:

$$n_s m_s\frac{\partial\mathbf{u}_s}{\partial t} = n_s q_s(\mathbf{E} + \mathbf{u}_s\times\mathbf{B}_0) \tag{A.2.1}$$

Using the linear wave approximation, equation (A.2.1) for a single species can be rewritten as

$$-i\omega m\mathbf{u}_1 = q(\mathbf{E}_1 + \mathbf{u}_1\times\mathbf{B}_0) \tag{A.2.2}$$

The scalar components of equation (A.2.2) can then be expressed as

$$\begin{aligned} -i\omega m u_x &= q(E_x + u_y B_0) \\ -i\omega m u_y &= q(E_y - u_x B_0) \\ -i\omega m u_z &= q E_z \end{aligned} \tag{A.2.3}$$

Then, solving for the particle velocity components from (A.2.3) gives

$$\begin{aligned} u_x &= \frac{q}{m}\left(\frac{i\omega E_x - \omega_c E_y}{\omega^2 - \omega_c^2}\right) \\ u_y &= \frac{q}{m}\left(\frac{i\omega E_y + \omega_c E_x}{\omega^2 - \omega_c^2}\right) \\ u_z &= \frac{iq}{\omega m} E_z \end{aligned} \tag{A.2.4}$$

Where the definition of the cyclotron frequency $\omega_c = qB_0/m$ has been used. Furthermore, note that

$$\mathbf{j}_1 = \sigma \cdot \mathbf{E}_1 = \sum_s q_s n_s \mathbf{u}_1 \tag{A.2.5}$$

Making use of (A.2.4), the conductivity tensor σ can then be written as

$$\sigma = \begin{bmatrix} \sigma_{xx} & \sigma_{xy} & 0 \\ \sigma_{yx} & \sigma_{yy} & 0 \\ 0 & 0 & \sigma_{zz} \end{bmatrix} \tag{A.2.6}$$

Where the elements are

$$\begin{aligned} \sigma_{xx} = \sigma_{yy} &= \sum_s \frac{q_s^2 n_s}{m_s} \frac{i\omega}{\omega^2 - \omega_{cs}^2} \\ \sigma_{xy} = -\sigma_{yx} &= -\sum_s \frac{q_s^2 n_s}{m_s} \frac{\omega_{cs}}{\omega^2 - \omega_{cs}^2} \\ \sigma_{zz} &= \sum_s \frac{i q_s^2}{m_s} \frac{n_s}{\omega} \end{aligned} \tag{A.2.7}$$

Given this new information, the definition of the dielectric tensor $\mathsf{K} = \mathbb{1} + (i/\epsilon_0\omega)\sigma$

can be written in the form

$$\mathsf{K} = \begin{bmatrix} S & -iD & 0 \\ iD & S & 0 \\ 0 & 0 & P \end{bmatrix} \tag{A.2.8}$$

Where the elements can be expressed as

$$\begin{aligned} S &= 1 - \sum_s \frac{\omega_{ps}^2}{\omega^2 - \omega_{cs}^2} \\ D &= \sum_s \frac{\omega_{cs}\omega_{ps}^2}{\omega\left(\omega^2 - \omega_{cs}^2\right)} \\ P &= 1 - \sum_s \frac{\omega_{ps}^2}{\omega^2} \end{aligned} \tag{A.2.9}$$

Where the S, D, and P represent the Sum, Difference, and Plasma terms that were made familiar by Stix and $\omega_p = q^2 n/\epsilon_0 m$ is the definition of the plasma frequency [21].

A.3 The Dispersion Relation

Before constructing the dispersion tensor, the remainder of equation (A.1.6) will be considered. First, let $\mathbf{k}$ lie in the x-z plane making an angle θ with the magnetic field vector $\mathbf{B}_0 = B_0\hat{\mathbf{z}}$ such that $\mathbf{k} = k\sin\theta\hat{\mathbf{x}} + k\cos\theta\hat{\mathbf{z}}$. Then the dyad $n^2\hat{\mathbf{k}}\hat{\mathbf{k}}$ can be expressed as

$$n^2\hat{\mathbf{k}}\hat{\mathbf{k}} = \begin{bmatrix} n^2\sin^2\theta & 0 & n^2\sin\theta\cos\theta \\ 0 & 0 & 0 \\ n^2\sin\theta\cos\theta & 0 & n^2\cos^2\theta \end{bmatrix} \tag{A.3.1}$$

and the tensor $n^2\mathbb{1}$ can be written as

$$-n^2\mathbb{1} = \begin{bmatrix} -n^2 & 0 & 0 \\ 0 & -n^2 & 0 \\ 0 & 0 & -n^2 \end{bmatrix}$$

$$= \begin{bmatrix} -n^2\left(\sin^2\theta + \cos^2\theta\right) & 0 & 0 \\ 0 & -n^2\left(\sin^2\theta + \cos^2\theta\right) & 0 \\ 0 & 0 & -n^2\left(\sin^2\theta + \cos^2\theta\right) \end{bmatrix} \tag{A.3.2}$$

Finally, by combining equations (A.1.6), (A.2.8), (A.3.1), and (A.3.2), the complete, cold plasma dispersion tensor can be written as

$$\mathsf{D} = \begin{bmatrix} S - n^2\cos^2\theta & -iD & n^2\sin\theta\cos\theta \\ iD & S - n^2 & 0 \\ n^2\sin\theta\cos\theta & 0 & P - n^2\sin^2\theta \end{bmatrix} \tag{A.3.3}$$

The non-trivial ($\mathbf{E}_1 \neq 0$) solutions of the cold plasma dispersion relation can be found by taking $\det \mathsf{D} = 0$ and solving for $\tan^2\theta$. Doing this yields

$$\left[S\sin^2\theta + P\cos^2\theta\right]n^4 - \left[RL\sin^2\theta + SP\left(1 + \cos^2\theta\right)\right]n^2 + PRL = 0$$

$$n^2\sin^2\theta + \frac{Pn^2\left(n^2 - S\right)}{Sn^2 - RL}\cos^2\theta - P\left(\sin^2\theta + \cos^2\theta\right) = 0$$

$$\left(n^2 - P\right)\sin^2\theta = -\frac{P\left(n^4 - 2Sn^2 + RL\right)}{Sn^2 - RL}$$

$$\tan^2\theta = -\frac{P\left(n^2 - R\right)\left(n^2 - L\right)}{\left(Sn^2 - RL\right)\left(n^2 - P\right)} \tag{A.3.4}$$

Where the R and L terms represent Right and Left and are related to the S and D

terms in the following manner:

$$\begin{aligned} R &= S + D \\ L &= S - D \\ S &= \frac{1}{2}(R + L) \\ D &= \frac{1}{2}(R - L) \end{aligned} \tag{A.3.5}$$

The form of the dispersion relation represented in equation (A.3.4) is very useful when considering the two primary sets of modes corresponding to $\theta = 0$ ($\mathbf{k} \parallel \mathbf{B}_0$) and $\theta = \pi/2$ ($\mathbf{k} \perp \mathbf{B}_0$).

Up to this point, the general cold plasma dispersion relation has been derived as an exercise in the theory of plasma waves. The results of this derivation could be used to look at the general dispersion relation of RCP and LCP waves for $\theta = 0$ in equation (A.3.4); however, these relations do not embody the character of the helicon–Trivelpiece-Gould (H-TG) mode coupling.

A.4 Helicon–Trivelpiece-Gould Theory

A.4.1 The H-TG Wave Equation: Cold Plasma Route

The H-TG wave equation will be derived formally from the theory presented in the previous section. Though a more direct route can be followed, this one allows the reader to understand the relationship to cold plasma theory. The reader should note that, from this point forward, the nomenclature for wavenumber will be changed to the helicon theory convention as adopted by Chen et. al. [10, 17]. The total wavenumber will be referred to as β, while the transverse and axial wavenumbers will be referred to as T and k, respectively. That is $\beta^2 = T^2 + k^2$. The author recognizes the potential for confusion in this case; however, it was felt that adhering to convention in context to helicon theory would be the best course of action for the purpose of orienting the reader to that which is found in the literature.

First, the right-hand side of equation (A.1.2) will be reconsidered. The total current can therefore be expressed as follows:

$$\mathbf{J}_1 = \mathbf{j}_{1p} + \mathbf{j}_{1d} = -i\omega\epsilon_0 \mathsf{K} \cdot \mathbf{E}_1 \tag{A.4.1}$$

Where the $\mathbf{j}_{1p}$ and $\mathbf{j}_{1d}$ are the first order plasma and displacement currents, respectively. Solving for $\mathbf{E}_1$, gives

$$-i\omega\epsilon_0 \mathbf{E}_1 = \mathsf{K}^{-1}\mathbf{J}_1$$

$$-i\omega\epsilon_0 \mathbf{E}_1 = \frac{1}{P}\mathbf{J}_1 - i\frac{D}{RL}\hat{\mathbf{b}} \times \mathbf{J}_1 + \left(\frac{1}{P} - \frac{S}{RL}\right)\hat{\mathbf{b}} \times \hat{\mathbf{b}} \times \mathbf{J}_1$$

$$\mathbf{E}_1 = -\frac{1}{i\omega\epsilon_0}\left[\alpha_p \mathbb{1} + i\alpha_h \hat{\mathbf{b}} \times -\alpha_d\left(\mathbb{1} - \hat{\mathbf{b}}\hat{\mathbf{b}}\right)\right] \cdot \mathbf{J}_1 \tag{A.4.2}$$

Where $RL = S^2 - D^2$, $\hat{\mathbf{b}} = \mathbf{b}/B_0 = \hat{\mathbf{z}}$ is a unit vector along the z-axis, and $\alpha_p = 1/P$, $\alpha_h = -D/RL$, and $\alpha_d = 1/P - S/RL$ represent the polarization, Hall, and displacement current coefficients, respectively, as adopted by Chen et. al. [10, 17]. Now, let us evaluate the coefficients so as to reduce equation (A.4.2) into a more useful form. In this derivation, a single ion species will be assumed and the displacement current $\mathbf{j}_{1d}$, will be neglected such that α_d will vanish; however, either of these simplifications can be omitted to reach a more complete form. The Right, Left, Sum, Difference, and Plasma elements can be expressed from equations (A.2.9) as

$$\begin{aligned}
R &= 1 - \frac{\omega_{pi}^2}{\omega\left(\omega + \omega_{ci}\right)} - \frac{\omega_{pe}^2}{\omega\left(\omega - \omega_{ce}\right)} \\
L &= 1 - \frac{\omega_{pi}^2}{\omega\left(\omega - \omega_{ci}\right)} - \frac{\omega_{pe}^2}{\omega\left(\omega + \omega_{ce}\right)} \\
S &= 1 - \frac{\omega_{pi}^2}{\omega^2 - \omega_{ci}^2} - \frac{\omega_{pe}^2}{\omega^2 - \omega_{ce}^2} \\
D &= \frac{\omega_{ci}\omega_{pi}^2}{\omega\left(\omega^2 - \omega_{ci}^2\right)} - \frac{\omega_{ce}\omega_{pe}^2}{\omega\left(\omega^2 - \omega_{ce}^2\right)} \\
P &= 1 - \frac{\omega_{pi}^2}{\omega^2} - \frac{\omega_{pe}^2}{\omega^2}
\end{aligned} \tag{A.4.3}$$

Now, by considering $\omega^2 \gg \omega_{ci}\omega_{ce} = \omega_{LH}^2$ equations (A.4.3) become

$$\begin{aligned} R &= 1 - \frac{\omega_{pe}^2}{\omega\left(\omega - \omega_{ce}\right)} \\ L &= 1 - \frac{\omega_{pe}^2}{\omega\left(\omega + \omega_{ce}\right)} \\ S &= 1 - \frac{\omega_{pe}^2}{\omega^2 - \omega_{ce}^2} \\ D &= -\frac{\omega_{ce}\omega_{pe}^2}{\omega\left(\omega^2 - \omega_{ce}^2\right)} \\ P &= 1 - \frac{\omega_{pe}^2}{\omega^2} \end{aligned} \tag{A.4.4}$$

Finally, the 1 vanishes in R, L, S, and P in the limit $\mathbf{j}_d \rightarrow 0$ giving

$$\begin{aligned} RL &= \frac{\omega_{pe}^4}{\omega^2 - \omega_{ce}^2} \\ S &= -\frac{\omega_{pe}^2}{\omega^2 - \omega_{ce}^2} \\ D &= -\frac{\omega_{ce}\omega_{pe}^2}{\omega\left(\omega^2 - \omega_{ce}^2\right)} \\ P &= -\frac{\omega_{pe}^2}{\omega^2} \end{aligned} \tag{A.4.5}$$

This gives $\alpha_p = -\omega^2/\omega_{pe}^2$ and $\alpha_h = \omega\omega_{ce}/\omega_{pe}^2$, which, when re-entered into equation (A.4.2) gives

$$\begin{aligned} \mathbf{E}_1 &= \frac{i}{\epsilon_0}\left[-\frac{\omega}{\omega_{pe}^2}\mathbb{1} + i\frac{\omega_{ce}}{\omega_{pe}^2}\hat{\mathbf{b}}\times\right]\cdot\mathbf{J}_1 \\ \mathbf{E}_1 &= -\frac{\omega_{ce}}{\omega_{pe}^2\epsilon_0}\left[i\delta\mathbb{1} - \hat{\mathbf{b}}\times\right]\cdot\mathbf{J}_1 \end{aligned} \tag{A.4.6}$$

Where $\delta = \omega/\omega_{ce}$. At this point, it is useful to note that equation (A.4.6) can be reached by combining equations (A.2.1) and (A.2.5) and manipulating the result. Furthermore, collisions can be considered easily by noting that equation (A.2.1) including the collision term $-m_s\nu_s\mathbf{u}_s$ on the right-hand side can be manipulated such

that equation (A.4.6) becomes

$$\mathbf{E}_1 = -\frac{\omega_{ce}}{\omega_{pe}^2 \epsilon_0} \left[i\delta^* \mathbb{1} - \hat{\mathbf{b}}\times \right] \cdot \mathbf{J}_1 \tag{A.4.7}$$

Where $\delta^* = (\omega + i\nu)/\omega_{ce}$ and in the limit $\nu \to 0$, $\delta^* \to \delta = \omega/\omega_{ce}$. At this point, it is useful to note that the Fourier transform in the time domain will be used, however, the spacial domain will remain unchanged. This is to say that all quantities can be expressed in the form $\mathbf{B}_1(\mathbf{r}, t) = Re\left[\mathbf{B}_1(\mathbf{r}, \omega)\, e^{-i\omega t}\right]$, in the case of the magnetic field. Using Faraday's Law, equation (A.4.7) can be written as

$$\nabla \times \mathbf{E}_1 = i\omega \mathbf{B}_1 = -\frac{\omega_{ce}}{\omega_{pe}^2 \epsilon_0} \left[i\delta^* \nabla \times - \nabla \times \hat{\mathbf{b}}\times \right] \cdot \mathbf{J}_1 \tag{A.4.8}$$

Furthermore, if Ampere's Law is applied, neglecting the displacement current and rearranging will show that equation (A.4.8) becomes

$$i\omega \mathbf{B}_1 = -\frac{\omega_{ce}}{\omega_{pe}^2 \epsilon_0 \mu_0} \left[i\delta^* \nabla \times - \nabla \times \hat{\mathbf{b}}\times \right] \nabla \times \mathbf{B}_1$$

$$\frac{\delta \omega_{pe}^2}{c^2} \mathbf{B}_1 = -\left[\delta^* \nabla \times + i \nabla \times \hat{\mathbf{b}}\times \right] \nabla \times \mathbf{B}_1$$

$$\delta^* \nabla \times \nabla \times \mathbf{B}_1 + i \nabla \times \hat{\mathbf{b}} \times (\nabla \times \mathbf{B}_1) + \frac{\delta \omega_{pe}^2}{c^2} \mathbf{B}_1 = 0$$

$$\delta^* \nabla \times \nabla \times \mathbf{B}_1 - k \nabla \times \mathbf{B}_1 + \delta k_s^2 \mathbf{B}_1 = 0 \tag{A.4.9}$$

Where $k_s = \omega_{pe}/c$ is called the skin depth by Chen et. al. [10, 17]. Equation (A.4.9) is the formal H-TG wave equation and will be used for the remainder of the analysis.

A.4.2 H-TG Waves

Equation (A.4.9) can now be factored into

$$(\beta_1 - \nabla\times)(\beta_2 - \nabla\times)\mathbf{B} = 0 \tag{A.4.10}$$

Where the first-order subscript $_1$ on $\mathbf{B}$ has been removed for the remainder of the analysis to eliminate confusion with the general solution.

The general solution of equation (A.4.10) is then found to be $\mathbf{B} = \mathbf{B}_1 + \mathbf{B}_2$ such that $\mathbf{B}_1$ and $\mathbf{B}_2$ satisfy the following equation for $j = 1, 2$:

$$\nabla \times \mathbf{B}_j = \beta_j \mathbf{B}_j \tag{A.4.11}$$

the curl of which can be written in the form of the Helmholtz wave equation for $j = 1, 2$ as

$$\nabla^2 \mathbf{B}_j + \beta_j^2 \mathbf{B}_j = 0 \tag{A.4.12}$$

The separation constants β_1 and β_2 are the roots of

$$\delta^* \beta^2 - k\beta + \delta k_s^2 = 0 \tag{A.4.13}$$

and the solutions to equation (A.4.13) can be expressed as

$$\beta_{1,2} = \frac{k}{2\delta^*} \left[1 \mp \left(1 - \frac{4\delta^* \delta k_s^2}{k^2} \right)^{\frac{1}{2}} \right] \tag{A.4.14}$$

In this case, β_1 represents the helicon branch and β_2 represents the TG branch. In order to simplify further analysis and make obvious the characteristics of these branches, collisions will be neglected from this point forward, thus $\delta^* = \delta$. As a result, an alternative form for equation (A.4.13) gives a useful expression for k in terms of β as follows:

$$k = \frac{\delta}{\beta} \left(\beta^2 + k_s^2 \right) \tag{A.4.15}$$

Next, by taking the minimum of equation (A.4.15), it is found that there exists a minimum k value in order for wave propagation to occur

$$k_{min} = 2\delta k_s \tag{A.4.16}$$

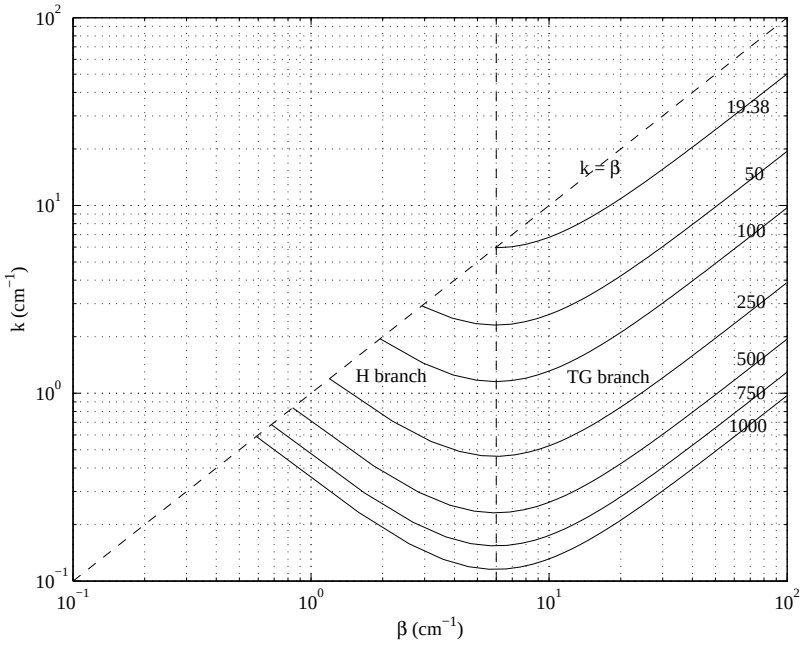

Figure A-1: A plot of k versus β for different values of $B_0(G)$ in a plasma of density $n_0 = 1 \times 10^{13}\ cm^{-1}$ and a rf frequency of 27.12 Mhz.

Furthermore, by defining the transverse wave number for $j = 1, 2$ in terms of the total and parallel wave numbers β and k as

$$T_j^2 = \beta_j^2 - k^2 \tag{A.4.17}$$

it is found that for real T_j there exists a maximum k value at $T = 0$ ($k = \beta$) of

$$k_{max} = k_s \sqrt{\frac{\delta}{1-\delta}} \tag{A.4.18}$$

So, as δ increases ($B_0 \to 0$), we see that k_{min} approaches k_{max} until the value $\delta = 2\omega/\omega_{ce}$ is reached. At this point, $k_{min} = k_{max}$ and the helicon wave no longer propagates. This behavior can be seen in Figure A-1. The H branch is to the left of the minimum while the TG branch is to the right. Note how the size of the H branch decreases for decreasing B_0 until it becomes evanescent at a magnetic field value of $B_0 \approx 19.38$ G for the given conditions.

A.4.3 Boundary Condition Effects

In order to study the effects of boundary conditions on the character of H-TG modes, equation (A.4.12) will be solved. The solution to the Helmholtz wave equation in circular cylindrical geometry can be found through use of the method of separation of variables. All perturbed quantities vary as $e^{i(m\phi+kz-\omega t)}$, where m is the mode number such that $m > 0$ and $m < 0$ represent clockwise and counterclockwise rotation, respectively when viewing the wave in the direction of $\mathbf{B}_0 = B_0\hat{\mathbf{z}}$. The z-component of equation (A.4.12) can be written in the form of the well known Bessel differential equation obtained by separating variables as $\mathbf{B}(r,\phi) = \mathbf{B}(r)\, e^{im\phi}$

$$\frac{\partial^2 B_{zj}}{\partial r^2} + \frac{1}{r}\frac{\partial B_{zj}}{\partial r} + \left(T_j^2 - \frac{m^2}{r^2}\right) B_{zj} = 0 \tag{A.4.19}$$

Where m is the mode number such that B_z depends on azimuthal angle ϕ as $e^{im\phi}$. The solution to equation (A.4.19) is finite for $r = 0$ and is written as

$$B_{zj} = C_1 J_m(T_j r) \tag{A.4.20}$$

Where $J_m(T_j r)$ is a Bessel function of the first kind of mode m.

Next, the r and ϕ components of (A.4.11) are

$$\frac{1}{r}\frac{\partial B_{zj}}{\partial \phi} - \frac{\partial B_{\phi j}}{\partial z} = \frac{im}{r} B_{zj} - ikB_{\phi j} = \beta_j B_{rj} \tag{A.4.21}$$

$$\frac{\partial B_{rj}}{\partial z} - \frac{\partial B_{zj}}{\partial r} = ikB_{rj} - \frac{\partial B_{zj}}{\partial r} = \beta_j B_{\phi j} \tag{A.4.22}$$

Then solving for B_{rj} and $B_{\phi j}$ in terms of B_{zj} and $\partial B_{zj}/\partial r$ gives

$$B_{rj} = \frac{iC_1}{T_j^2}\left[\frac{m}{r}\beta_j J_m(T_j r) - k\frac{\partial}{\partial r} J_m(T_j r)\right] \tag{A.4.23}$$

$$B_{\phi j} = \frac{C_1}{T_j^2}\left[\frac{m}{r} k J_m(T_j r) + \beta_j \frac{\partial}{\partial r} J_m(T_j r)\right] \tag{A.4.24}$$

Finally, using the recursion relations for $J_m(T_j r)$ and $\partial J_m(T_j r)/\partial r$

$$\begin{aligned} \frac{m}{r} J_m(T_j r) &= \frac{T_j}{2}\Big[J_{m-1}(T_j r) + J_{m+1}(T_j r)\Big] \\ \frac{\partial}{\partial r} J_m(T_j r) &= \frac{T_j}{2}\Big[J_{m-1}(T_j r) - J_{m+1}(T_j r)\Big] \end{aligned} \tag{A.4.25}$$

equations (A.4.23), (A.4.24), and (A.4.20) can be written in their final form as

$$B_{rj} = A_j\Big[(\beta_j + k)\, J_{m-1}(T_j r) + (\beta_j - k)\, J_{m+1}(T_j r)\Big] \tag{A.4.26}$$

$$B_{\phi j} = iA_j\Big[(\beta_j + k)\, J_{m-1}(T_j r) - (\beta_j - k)\, J_{m+1}(T_j r)\Big] \tag{A.4.27}$$

$$B_{zj} = -2iT_j A_j J_m(T_j r) \tag{A.4.28}$$

Where $A_j = iC_1/2T_j$ is an arbitrary amplitude.

Now a similar procedure can be performed for $\mathbf{E}_j$. First, equations (A.1.2) and (A.4.11) will be considered, while neglecting displacement current. From these, it is found

$$\mathbf{j}_j = \frac{\beta_j}{\mu_0}\mathbf{B}_j \tag{A.4.29}$$

Next, using equation (A.4.6), an expression for $\mathbf{E}_j$ as a function of $\mathbf{B}_j$ can be found as follows:

$$\mathbf{E}_j = -\frac{\omega_{ce}\beta_j}{k_s^2}\Big[i\delta\mathbb{1} - \hat{\mathbf{b}}\times\Big]\cdot\mathbf{B}_j \tag{A.4.30}$$

Writing E_{zj} from equation (A.4.30) and using equation (A.1.1) for the r and ϕ components gives

$$E_{zj} = -\frac{i\omega\beta_j}{k_s^2}B_{zj} \tag{A.4.31}$$

$$\frac{1}{r}\frac{\partial E_{zj}}{\partial\phi} - \frac{\partial E_{\phi j}}{\partial z} = -\frac{m}{r}\frac{i\omega\beta_j}{k_s^2}B_{zj} - ikE_{\phi j} = i\omega B_{rj} \tag{A.4.32}$$

$$\frac{\partial E_{rj}}{\partial z} - \frac{\partial E_{zj}}{\partial r} = ikE_{rj} + \frac{i\omega\beta_j}{k_s^2}\frac{\partial B_{zj}}{\partial r} = i\omega B_{\phi j} \tag{A.4.33}$$

Solving for E_{rj} and $E_{\phi j}$ and including equation (A.4.31) gives the complete set of

E wave field equations in terms of the components of **B**

$$E_{rj} = \frac{\omega}{k} B_{\phi j} - \frac{\omega \beta_j}{k_s^2} \frac{\partial B_{zj}}{\partial r} \tag{A.4.34}$$

$$E_{\phi j} = -\frac{\omega}{k} B_{rj} - \frac{m}{r} \frac{\omega \beta_j}{k_s^2} B_{zj} \tag{A.4.35}$$

$$E_{zj} = -\frac{i\omega \beta_j}{k_s^2} B_{zj} \tag{A.4.36}$$

Now, the H-TG coupling due to a conducting cylinder boundary and an insulating cylinder boundary can be examined. When $m_e \to 0$, $\omega_{pe} \to \infty$ and $k_s \to \infty$ and so it is found that these conditions are simplified greatly due to the fact that $E_z \to 0$ from equation (A.4.36). From this, only $E_\phi = 0$ for a conducting cylinder and it follows from equation (A.4.35) that $B_r = 0$. Next, for an insulating cylinder, the boundary condition $j_r = 0$ must be satisfied. From equation (A.4.29), this implies that $B_r = 0$, which in turn forces $E_\phi = 0$ from equation (A.4.35). Thus, the boundary conditions for both a conducting and an insulating cylinder are the same in the case of zero-electron mass. This was first shown by Chen [10].

From this study, in can be seen that there is only one condition necessary for both boundary types, namely:

$$B_{r1} = A_1 \Big[(\beta_1 + k) J_{m-1}(T_1 a) + (\beta_1 - k) J_{m+1}(T_1 a) \Big] = 0 \tag{A.4.37}$$

Where a is the bounding cylinder radius and β_1 is found to be

$$\beta_1 = \frac{\delta k_s^2}{k} = \frac{\omega}{k} \frac{n_0 q \mu_0}{B_0} \tag{A.4.38}$$

Note that equation (A.4.38) is the only solution to equation (A.4.13) in the $m_e = 0$ situation, thus the H branch is the only existing wave. Equation (A.4.38) is also the dispersion relation for unbound, ionospheric whistler waves, emphasizing the fact that helicon waves are simply bounded whistler waves.

If the electron mass is now taken to be finite, then it follows that E_z must be finite

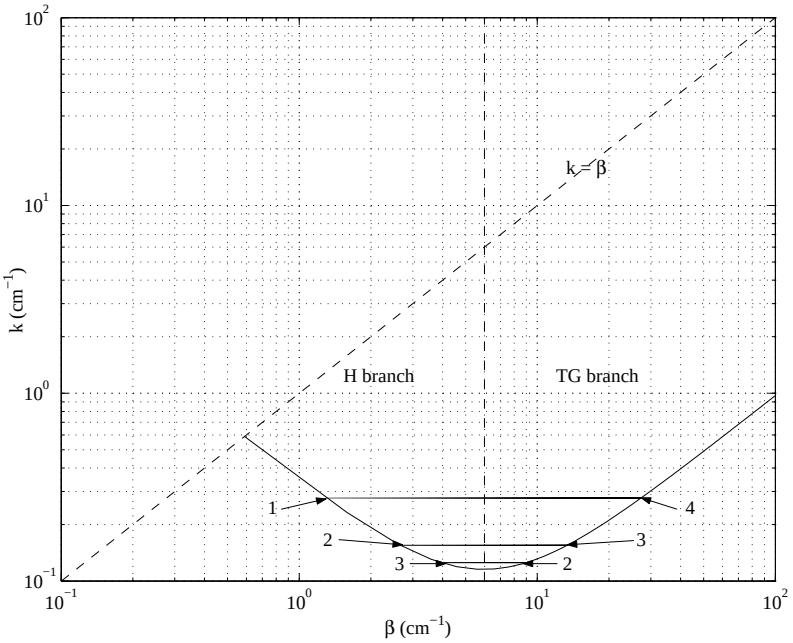

Figure A-2: A plot of k versus β for $B_0 = 1000\ G$ in a plasma of density $n_0 = 1 \times 10^{13}\ cm^{-1}$ and a rf frequency of 27.12 Mhz showing the discretized values of k for which H-TG modes can propagate. Note that only the first three modes can be resolved at this scale.

due to electron inertia regardless of collisions [10]. Therefore, in order for $E_z = 0$, the condition $\sum_{j=1,2} \beta_j B_{zj} \to 0$ as $r \to a$ must be satisfied. If $E_{zj} = 0$ is imposed for both waves, then from equation (A.4.28), it is found that

$$\beta_j J_m(T_j a) = 0 \tag{A.4.39}$$

The two waves cannot, in general, satisfy this condition separately, so the $E_{zj} = 0$ condition couples the two waves. Using equations (A.4.28) and (A.4.30) and setting $E_z = E_{z1} + E_{z2} = 0$ the ratio of the two wave amplitudes is found as

$$\frac{A_2}{A_1} = -\frac{\beta_1 J_m(T_1 a) T_1}{\beta_2 J_m(T_2 a) T_2} \tag{A.4.40}$$

Again, since $E_{\phi j} = 0$ is a necessary condition, then from equation (A.4.35) it is

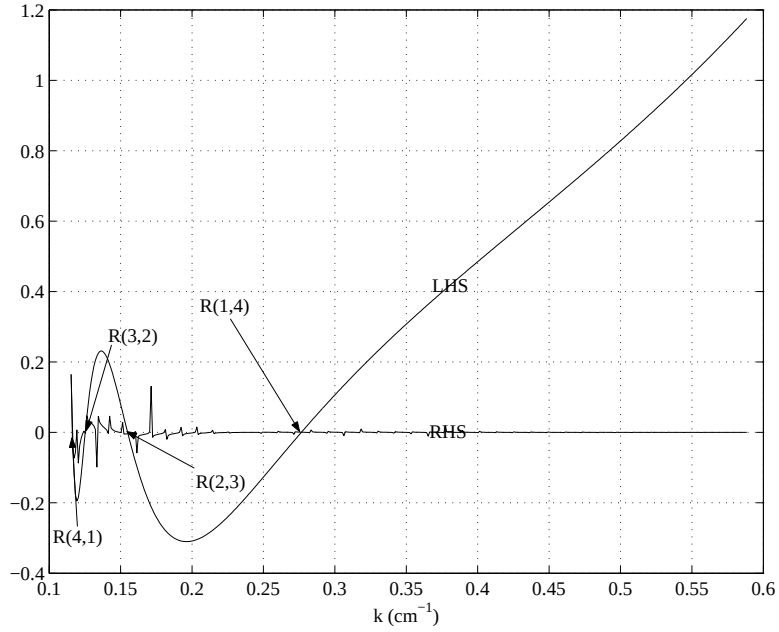

Figure A-3: A plot of the LHS and RHS of equation (A.4.42) versus k for $B_0 = 1000\ G$ in a plasma of density $n_0 = 1 \times 10^{13}\ cm^{-1}$ and a rf frequency of 27.12 Mhz. The modes can clearly be seen as the intersections of the two functions.

found that $\sum_j B_{rj} = 0$ required to satisfy that condition. Using equation (A.4.26), the amplitude ratio can be written as

$$\frac{A_2}{A_1} = -\frac{(\beta_1 + k)\, J_{m-1}(T_1 a) + (\beta_1 - k)\, J_{m+1}(T_1 a)}{(\beta_2 + k)\, J_{m-1}(T_2 a) + (\beta_2 - k)\, J_{m+1}(T_2 a)} \tag{A.4.41}$$

From the general theory of plasma waves, it is known that waves in a bounded plasma differ from those found in an infinite plasma in that the range of k for wave propagation becomes discretized rather than continuous. This case now becomes clear in that equations (A.4.40) and (A.4.41) can only be simultaneously satisfied for certain values of k. Thus, the full version of this boundary condition can be written

as

$$\Big[(\beta_1 + k)\, J_{m-1}(T_1 a) + (\beta_1 - k)\, J_{m+1}(T_1 a) \Big] = \Big[(\beta_2 + k)\, J_{m-1}(T_2 a) + (\beta_2 - k)\, J_{m+1}(T_2 a) \Big] \frac{\beta_1 J_m(T_1 a) T_1}{\beta_2 J_m(T_2 a) T_2} \quad \text{(A.4.42)}$$

This allows for the determination of the discrete values of k for which modes exist. The lowest radial H mode is given by the highest k value and corresponds to the highest radial TG mode. The notation $R(n_H, n_{TG})$ will be used to denote the different coupled mode numbers.

Figure A-2 illustrates the discrete nature of the H-TG waves in cylindrically bounded geometry for a conducting surface. By plotting the LHS and RHS of equation (A.4.42) versus k over the range of k_{min} to k_{max}, the reader can get a graphical feel for the values of k which satisfy the boundary condition. Though there are four modes in total as can be seen in the case of Figure A-3, Chen et. al. [10, 16, 17, 18] have found in experiments that only the lowest radial H mode is physically observed.

For large B_0 at the lowest radial H mode, it can seen that $\beta_2 \gg \beta_1$. Furthermore, equation (A.4.31) states that β_2 is proportional to E_{z2}/B_{z2}, therefore the TG wave is electrostatic and has a high radial frequency. In fact, Chen et. al. [10, 16, 17, 18] have shown that at the lowest radial H mode, the $m_e = 0$ approximation is sufficient for description of behavior and the TG wave can be neglected. However, as B_0 decreases it is found that the magnitude of the electromagnetic component of the TG wave increases so that both waves must be considered.

Appendix B

A Helicon Fluid Model

B.1 Properties of a Helicon Plasma

In this section, the typical values of quantities of interest in a helicon plasma will be introduced. These will be used to calculate some characteristic frequencies of the physical system, which will then be compared in an attempt to establish an appropriate physical model for our system. All physical quantities were taken from Bose et. al. [19] and are typical of semiconductor and materials processing argon helicon plasmas.

Where B_0 is the externally applied, DC magnetic field, a is the radius of the cylindrical plasma column, and f_{RF} is the antenna excitation frequency.

Quantity	**Value**
$n_e = n_i = n$	10^{18} m^{-3}
T_e	3 eV
T_i	0.2 eV
Z_{Ar}	18
m_{Ar^+}	6.67×10^{-26} kg
B_0	100 G
a	0.04 m
f_{RF}	13.56×10^6 Hz

Table B.1: Quantities of interest for a typical helicon plasma.

In order to ensure the completeness of the comparison, the full non-linear momentum equation for species j will be considered; however, the model will be linearized to simplify its numerical treatment and so it is comparable to previous analytical work.

$$m_j n_j \left(\frac{\partial \mathbf{u}_j}{\partial t} + (\mathbf{u}_j \cdot \nabla)\, \mathbf{u}_j \right) = q_j n_j \left(\mathbf{E} + \mathbf{u}_j \times \mathbf{B}_0 \right) - \nabla p_j - m_j n_j \nu_j \mathbf{u}_j \tag{B.1.1}$$

For convenience, this can be recast in the following form:

$$n_j \left(\frac{\partial \mathbf{u}_j}{\partial t} + (\mathbf{u}_j \cdot \nabla)\, \mathbf{u}_j \right) = \frac{q_j n_j}{m_j} \mathbf{E} - n_j \left(\omega_{cj} \times \mathbf{u}_j \right) - \frac{\nabla p_j}{m_j} - n_j \nu_j \mathbf{u}_j \tag{B.1.2}$$

In order to determine the predominant physical mechanisms in the helicon plasma, the inertial, convective, magnetic, and collision terms in equation (B.1.2) must be compared, where the terms are given, respectively, as follows:

$$\begin{aligned} \frac{\partial \mathbf{u}_j}{\partial t} &\propto f_{RF} \\ (\mathbf{u}_j \cdot \nabla)\, \mathbf{u}_j &\propto \frac{u}{a} \\ \omega_c \times \mathbf{u}_j &\propto \omega_{cj} \\ \nu_j \mathbf{u}_j &\propto \nu_j \end{aligned} \tag{B.1.3}$$

The characteristic frequencies can then be computed with the following equations:

$$\begin{aligned} \frac{u}{a} &= \sqrt{\frac{2T_e}{m_i a^2}} \\ \omega_{ce} &= \frac{eB_0}{m_e} \\ \omega_{ci} &= \frac{ZeB_0}{m_i} \\ \nu_e &= 2.91 \times 10^{-6} n_e T_e^{-3/2} \ln\Lambda \\ \nu_i &= 4.80 \times 10^{-8} n_i T_e^{-3/2} Z^4 \left(\frac{m_p}{m_i} \right)^{1/2} \ln\Lambda \end{aligned} \tag{B.1.4}$$

where $\ln\Lambda$ is the Coulomb logorithm and m_p is the rest mass of a proton. Note that both the electron and ion velocity gradients are calculated using the ion Bohm

Frequency (Hz)	**Electron**	**Ion**
f_{RF}	1.4×10^7	1.4×10^7
$\frac{u}{a}$	9.5×10^4	9.5×10^4
f_c	2.8×10^8	6.9×10^4
ν	5.6×10^6	1.3×10^{10}

Table B.2: Electron and ion characteristic frequencies for a typical helicon plasma.

velocity under the assumption of quasi-neutrality. The practical equations for collision frequencies, ν_j are found by evaluating the physical constants multiplying the density and temperature terms [35].

Using the abovementioned plasma quantities from table B.1, the electron and ion characteristic frequencies are computed as shown in table B.2. Note that the cyclotron frequencies have been converted from angular frequencies, ω_c to temporal frequencies, f_c to remain consistent with the other values.

B.2 The Ion Fluid

First, the zeroth-order ion fluid will be considered. Notice that the magnitude of the collision term is much greater than any of the other terms. From this, it can be assumed that the inertial, convective, and magnetic field terms are negligible and can be omitted from the model without significant loss of physics. Now, equation (B.1.2) for ions can be rewritten by taking into consideration the above assumptions. The momentum equation becomes

$$n_j \mathbf{u}_i = \frac{q_i n_i}{\nu_i m_i} \mathbf{E} - \frac{\nabla p_i}{\nu_i m_i} \tag{B.2.1}$$

Where the ion flux vector can be defined as $\mathbf{\Gamma}_i = n_i \mathbf{u}_i$, the ion diffusion coefficient $D_i = kT_i/\nu_i m_i$, and the ion mobility $\mu_i = q_i/\nu_i m_i$ such that equation (B.2.1) can be rewritten in the form

$$\mathbf{\Gamma}_i = \mu_i n_i \mathbf{E} - \frac{D_i}{kT_i} \nabla p_i \tag{B.2.2}$$

Combining equation (B.2.2) with the ion mass continuity equation gives the following drift-diffusion equation for ions:

$$\frac{\partial \mathbf{n}_i}{\partial t} + \nabla \cdot \mathbf{\Gamma_i} = S_i \tag{B.2.3}$$

Where S_i is the ion source term and will be treated later.

B.3 The Electron Fluid

Now considering the zeroth-order electron fluide and referring back to table B.2, it can be seen that, aside from the convective term, all other terms are within one order of magnitude of each other. From this, only the convective term can be removed from the model. This leaves the following equation for the electron momentum:

$$n_e \frac{\partial \mathbf{u}_e}{\partial t} + n_e \nu_e \mathbf{u}_e - n_e \left(\omega_{ce} \times \mathbf{u}_e\right) = -\frac{e n_e}{m_e}\mathbf{E} - \frac{\nabla p_e}{m_e} \tag{B.3.1}$$

Defining the electron flux vector as $\mathbf{\Gamma}_e = n_e \mathbf{u}_e$, equation (B.3.1) can be rewritten as

$$\frac{\partial \mathbf{\Gamma}_e}{\partial t} + \nu_e \mathbf{\Gamma}_e - \left(\omega_{ce} \times \mathbf{\Gamma}_e\right) = -\frac{e}{m_e}\mathbf{E} - \frac{\nabla p_e}{m_e} \tag{B.3.2}$$

Notice that the right-hand side of equation (B.3.2) is just the steady-state electron flux vector, $\mathbf{\Gamma}_e$ in the absence of an external magnetic field, which will now be denoted with a superscript zero. Also, the left-hand side of the equation can be rewritten as a tensor multiplying the total electron flux vector. This gives the following equation:

$$\mathsf{G} \cdot \mathbf{\Gamma}_e = \mathbf{\Gamma}_e^0 \tag{B.3.3}$$

Where

$$\mathsf{G} = \left[\left(1 - i\frac{\omega}{\nu_e}\right)\mathbb{1} - \frac{1}{\nu_e}\omega_{ce}\times\right]$$

Finally by inverting the tensor G, the total electron flux vector, $\mathbf{\Gamma}_e$ in the presence

of a magnetic field is found to be

$$\mathbf{\Gamma}_e = \frac{1}{1+\frac{\omega_{ce}^2}{\nu_e^2}} \begin{bmatrix} 1+\frac{\omega_{cer}^2}{\nu_e^2} & \frac{\omega_{cer}\omega_{ce\theta}}{\nu_e^2} - \frac{\omega_{cez}}{\nu_e} & \frac{\omega_{cer}\omega_{cez}}{\nu_e^2} + \frac{\omega_{ce\theta}}{\nu_e} \\ \frac{\omega_{cer}\omega_{ce\theta}}{\nu_e^2} + \frac{\omega_{cez}}{\nu_e} & 1+\frac{\omega_{ce\theta}^2}{\nu_e^2} & \frac{\omega_{ce\theta}\omega_{cez}}{\nu_e^2} - \frac{\omega_{cer}}{\nu_e} \\ \frac{\omega_{cer}\omega_{cez}}{\nu_e^2} - \frac{\omega_{ce\theta}}{\nu_e} & \frac{\omega_{ce\theta}\omega_{cez}}{\nu_e^2} + \frac{\omega_{cer}}{\nu_e} & 1+\frac{\omega_{cez}^2}{\nu_e^2} \end{bmatrix} \cdot \mathbf{\Gamma}_e^0 \tag{B.3.4}$$

Notice that, as with the ions, equation (B.3.4) need only be combined with the electron mass continuity equation to get the electron drift-diffusion equation

$$\frac{\partial \mathbf{n}_e}{\partial t} + \nabla \cdot \mathbf{\Gamma_e} = S_e \tag{B.3.5}$$

B.4 Closure

At this point, all that must be done to complete the system is to include the coupling of the plasma to the helicon antenna, which is achieved by simply including the first-order (perturbation) system consisting of the wave equation, the antenna current, and conductivity tensor to the zeroth-order (equilibrium) system ion and electron diffusion equations along with appropriate boundary conditions

Zeroth-order:

$$\frac{\partial \mathbf{n}_i}{\partial t} + \nabla \cdot \mathbf{\Gamma_i} = S_i \tag{B.4.1}$$

$$n_i \mid_{r=a} = 0 \tag{B.4.2}$$

$$\frac{\partial \mathbf{n}_e}{\partial t} + \nabla \cdot \mathbf{\Gamma_e} = S_e \tag{B.4.3}$$

$$n_e \mid_{r=a} = 0 \tag{B.4.4}$$

$$\mathbf{\Gamma}_e = \frac{1}{1+\frac{\omega_{ce}^2}{\nu_e^2}} \begin{bmatrix} 1+\frac{\omega_{cer}^2}{\nu_e^2} & \frac{\omega_{cer}\omega_{ce\theta}}{\nu_e^2} - \frac{\omega_{cez}}{\nu_e} & \frac{\omega_{cer}\omega_{cez}}{\nu_e^2} + \frac{\omega_{ce\theta}}{\nu_e} \\ \frac{\omega_{cer}\omega_{ce\theta}}{\nu_e^2} + \frac{\omega_{cez}}{\nu_e} & 1+\frac{\omega_{ce\theta}^2}{\nu_e^2} & \frac{\omega_{ce\theta}\omega_{cez}}{\nu_e^2} - \frac{\omega_{cer}}{\nu_e} \\ \frac{\omega_{cer}\omega_{cez}}{\nu_e^2} - \frac{\omega_{ce\theta}}{\nu_e} & \frac{\omega_{ce\theta}\omega_{cez}}{\nu_e^2} + \frac{\omega_{cer}}{\nu_e} & 1+\frac{\omega_{cez}^2}{\nu_e^2} \end{bmatrix} \cdot \mathbf{\Gamma}_e^0 \tag{B.4.5}$$

First-order:

$$\nabla\left(\nabla\cdot\mathbf{E}\right)-\nabla^2\mathbf{E}-\frac{\omega^2}{c^2}\mathbf{E}+i\omega\mu_0\sigma\cdot\mathbf{E}=-i\omega\mu_0\mathbf{J_{antenna}} \tag{B.4.6}$$

$$\mathbf{J_{antenna}}=\mathbf{I_0}\delta\left(r-a\right)\delta\left(z-a\psi\tan\theta\right)\left[\cos^2\theta\cdot\hat{\psi}+\sin\theta\cos\theta\cdot\hat{z}\right] \tag{B.4.7}$$

$$\sigma=\frac{e^2n_e}{m_e\left(\nu-i\omega\right)}\frac{1}{1+\frac{\omega_{ce}^2}{\left(\nu-i\omega\right)^2}}\begin{bmatrix}1+\frac{\omega_{cer}^2}{\left(\nu-i\omega\right)^2} & \frac{\omega_{cer}\omega_{ce\theta}}{\left(\nu-i\omega\right)^2}-\frac{\omega_{cez}}{\left(\nu-i\omega\right)} & \frac{\omega_{cer}\omega_{cez}}{\left(\nu-i\omega\right)^2}+\frac{\omega_{ce\theta}}{\left(\nu-i\omega\right)}\\ \frac{\omega_{cer}\omega_{ce\theta}}{\left(\nu-i\omega\right)^2}+\frac{\omega_{cez}}{\left(\nu-i\omega\right)} & 1+\frac{\omega_{ce\theta}^2}{\left(\nu-i\omega\right)^2} & \frac{\omega_{ce\theta}\omega_{cez}}{\left(\nu-i\omega\right)^2}-\frac{\omega_{cer}}{\left(\nu-i\omega\right)}\\ \frac{\omega_{cer}\omega_{cez}}{\left(\nu-i\omega\right)^2}-\frac{\omega_{ce\theta}}{\left(\nu-i\omega\right)} & \frac{\omega_{ce\theta}\omega_{cez}}{\nu_e^2}+\frac{\omega_{cer}}{\nu_e} & 1+\frac{\omega_{cez}^2}{\left(\nu-i\omega\right)^2}\end{bmatrix}\cdot\mathbf{\Gamma}_e^0 \tag{B.4.8}$$

Equations (B.4.1) through (B.4.8) constitute the full helicon fluid model. The reader should note that the zeroth-order equations are steady-state or equilibrium equations for the ion and electron fluids; however, the first-order equations represent the time-dependent portion of the system. This is to say that the first-order equations represent the perturbed quantities as a result of application of the time-dependent antenna current in the model. Equation (B.4.7) represents the time-dependent forcing term for the wave equation (B.4.6) and is the result of the mathematical application of a helical, line current model of a half-wavelength helicon antenna.

Appendix C

Helicon Source Design

C.1 Plasma Parameters

Recall the helicon dispersion relation (A.4.38) as follows:

$$\beta_1 = \frac{\delta k_s^2}{k} = \frac{\omega}{k}\frac{n_0 q \mu_0}{B_0} \tag{C.1.1}$$

Where n_0 is the equilibrium plasma number density and B_0 is the DC magnetic field intensity. Furthermore the total wave number, β can be expressed in terms of the axial and transverse wave numbers as is seen in equation (A.4.17).

Chen et. al. [15] has shown that k^2 can be neglected relative to T^2 for helicon sources that are sufficiently long and thin. This allows $\beta \approx T$ to be assumed in the treatment of the source design, thus allowing equation A.4.38 to be rewritten as

$$\frac{\omega}{k} = \frac{TB_0}{n_0 e \mu_0} = \frac{3.83 B_0}{a n_0 e \mu_0} \tag{C.1.2}$$

The first result in equation (C.1.2) is replaced with the final, right-hand side result through application of the boundary condition $J_1(Ta) \approx 0$, where a is taken to be the tube radius and only the lowest order root is used.

Now, to begin the design process, an axial phase velocity, ω/k and a tube radius,

a must be chosen. Chen et. al. [10] makes note that the source can be designed in one of two ways. First by choosing the axial phase velocity to be close to the thermal velocity, v_{th}, the wave would be strongly damped by the Landau damping mechanism. The second option would be to choose the axial phase velocity to be near the ionizing-electron velocity. This follows Chen's notion that the advantage of helicons is the direct acceleration of primaries by wave-particle interaction.

If it is decided to match the phase velocity to the velocity of the ionizing electrons, then equation (C.1.2) can be rewritten in the following form:

$$\frac{\omega}{k} = \lambda f = \left(\frac{2eE}{m}\right)^{\frac{1}{2}} = \frac{3.83B_0}{an_0e\mu_0}$$

$$\frac{B_G}{n_{13}} = 31.2E^{\frac{1}{2}}a_{cm} \tag{C.1.3}$$

Equation has been put in terms of useful quantities to ease the design process. In the final result, E is the electron energy (eV) that is chosen to match the phase velocity, B_G represents the magnetic field intensity in Gauss, n_{13} is the number density in $10^{13}cm^{-3}$, and a_{cm} is the tube radius in centimeters. At this point, it can be seen that E is fixed by the type of gas chosen and, assuming that the designers have a target number density in mind and an upper limit on the size of the magnetic system, the tube radius can be readily calculated.

C.2 Antenna Design

Next, the antenna is considered and a discussion is made of how the above method can be applied to its design. Helicon antennae have coupling coefficients that scale as the square of the ratio of the transverse and axial wave numbers. The antenna aspect ratio can be defined to be

$$R = \frac{T}{k} = \frac{3.83}{a}\frac{\lambda}{2\pi} = 0.61\frac{\lambda}{a} \tag{C.2.1}$$

Where λ denotes the antenna length. From equation (C.2.1) it can be seen that the square of the aspect ratio, R is actually the antenna gain, which is a ratio of transverse and axial wave field intensities under the antenna. This means that a gain of 100 would produce transverse field intensities 100 times greater than the corresponding axial field intensities. This value ultimately relates to a given antenna's ability to ionize the working fluid, as initially it will operate as a capacitively-coupled discharge for purposes of ionization.

From here, an aspect ratio is chosen, giving λ in terms of the tube radius, a, which in turn, can be input into equation (C.1.3) and, along with the electron energy and the desired values of magnetic intensity and number density, will produce the required frequency.

As a relavent example, a typical helicon discharge in argon with a peak energy of $E = 30\ eV$, a target density of $1 \times 10^{13}\ cm^{-3}$, and a tube radius of $1\ cm$ will be considered. Let an antenna aspect ratio of 10 be chosen, which gives a gain of 100. Now, using equations (C.1.3) and (C.2.1) gives a value of antenna length, $\lambda = 16.39a$ and a phase velocity of $\lambda f = 3.25 \times 10^6\ m/s$. The final result is a required operating frequency of approximately $f = 19.82 \times 10^6\ Hz$ with a magnetic field intensity of approximately 170 G.

It is readily apparent that the method is one of simplicity that draws upon the helicon dispersion relation as a basis. The abovementioned design equations can be used in a variety of ways depending on the known parameters in a given design. Also, the designer may choose to tune the wave phase velocity to a different value rather than to the velocity of the primary electrons if this is so desired.

Appendix D

Surface Thermocouple Bonding

D.1 Surface Preparation

Both the quartz and alumina ceramic source tubes should first be prepared by cleaning them thoroughly with isopropyl alcohol to remove any grease, dirt, or other contaminants that might compromise the integrity of the epoxy bond. The tubes should then be left to air dry to ensure that all of the alcohol has evaporated. As mentioned in Chapter 5, each tube is separated into five cells. The three central cells have their respective thermocouples bonded to their center locations in a linear array, such that all thermocouple nodes are collinear as shown in figure 5-3. These locations were measured very precisely using a ruler having 1/32-inch accuracy, thus allowing a very accurate placement of the thermocouples. A regular pen or dry-erase marker can be used to mark the boundaries of the cells as well as the locations of the thermocouples on the tube. The author found it most useful to place the quartz tube on a white background thus allowing the markings to be readily seen through the tube when placing the thermocouples.

Figure D-1: A photograph of a properly mixed batch of OB-200 epoxy adhesive.

D.2 Epoxy Preparation

The Omega Engineering, Inc OmegaBond 200 High Temperature, High Thermal Conductivity Epoxy Adhesive is relatively simple to mix. The reader should use a flat glass or plastic vessel or surface on which to mix the resin and catalyst. The author used a simple flat piece of plastic as it was easy to transport during the bonding process and was able to be discarded up completion of the process. A wooden or plastic mixing stick can be used for each of the two components. The reader should note that this epoxy mixture presents inhalation as well as contact hazards and should work with it only in a well ventilated area and with proper hand and eye protection.

At room temperature, the catalyst is typically hard and not able to be manipulated for purposes of mixing. A simple 100 - 150 degree Fahrenheit water bath can be used to immerse the catalyst bottle and heat its contents to a more liquid state. Even upon heating, the catalyst will tend to have a hard surface coating which must be broken up and mixed in thoroughly before combining with the resin. The resin itself is a thick, grease-like consistency at room temperature and does not require any preparation

Figure D-2: A photograph of the quartz tube and thermocouples in the oven during a curing session.

prior to use.

The ratio of resin to catalyst suggested is 10:1 by weight. This can be easily measured using a typical digital laboratory or kitchen scale. The author used a digital kitchen scale and prepared batches of epoxy adhesive whose total weight was approximately 110 grams. This is typically more than enough for a single thermocouple array application and a great deal of excess will remain upon completion of the bonding. Thoroughly mixing the resin and the catalyst is of utmost importance for a homogeneous mixture of adhesive that will maintain its bonding properties during and after curing. The author has made many test batches where mixing was not done thoroughly enough and the result was a bad bond or visual inconsistencies in the resulting adhesive. The proper consistency and color of the mixture is shown for reference in figure D-1.

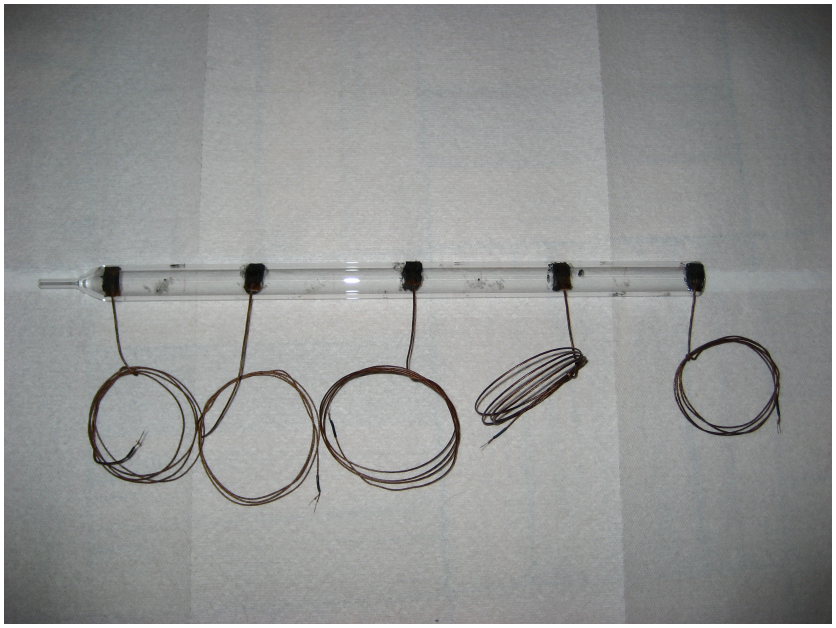

Figure D-3: A photograph of the quartz tube after having the thermocouples bonded to it and properly cured.

D.3 Thermocouple Bonding and Curing

After having cleaned the source tube and properly prepared the epoxy, the bonding of the thermocouples can be done. This is a tedious and often messy and frustrating process as the epoxy lacks heavy tackiness and so the small weight of the thermocouples can sometimes pry them loose from the tube surface before bonding is complete. It is important to note that as long as the actual thermocouple junction is bonded securely to the tube, the remaining Kapton sheet that may not be bonded should have a minimal impact on experimental results. Using laboratory latex gloves, the user should spread a small amount of epoxy on the surface of the thermocouple and ensure that it is evenly, though thinly coated. To apply the thermocouple to the tube requires a slight pressure, which ensures that the epoxy has formed a uniform and air-pocket free bond. Any excess epoxy should be attempted to be removed; however, in practice this tends more times than not to be far more difficult than expected. As can be seen in figure D-2, a natural gas-fired kitchen oven was used to cure the

thermocouple array and the tube itself was placed on a oven tray with aluminum foil covering it. While the epoxy manufacturer gives a variety of different temperatures and times for which the epoxy can be cured, the author has found the best results by curing for 2 hours at a temperature of 400 degrees Fahrenheit. A finished quartz tube with thermocouples properly bonded is shown in figure D-3.

Bibliography

[1] G. Sutton and O. Biblarz, Rocket Propulsion Elements, 7th Edition. Wiley-Interscience, 2000.

[2] M. Martínez-Sánchez, 16.522: Space Propulsion, Course notes. Massachusetts Institute of Technology, 2006.

[3] F.F. Chen, Plasma Physics and Control Fusion, 33, 339 (1991).

[4] R.W.Boswell, Phys. Lett. **33A**, 457 (1970).

[5] F.F. Chen, J.D. Evans, and G.R. Tynan, Design and performance of distributed helicon sources, Plasma Sources Sci. Technol. **10**, 236 (2001); UCLA LTP-008 (August, 2000).

[6] F. Chang-Díaz et al., Bull. APS **45** (7) 129, 2000.

[7] F. Chang-Díaz, The VASIMR Engine, Scientific American, 283 (5) 90, 2000.

[8] J. P. Squire et al., IAC-02-S.4.03, 53rd International Astronautical Congress, Houston TX, October 10-19, 2002.

[9] V.T. Jacobson et. al. Development of VASIMR helicon source, 43^{rd} Annual Meeting, APS Division of Plasma Science. (2001).

[10] F.F. Chen, Helicon Plasma Sources, in "High Density Plasma Sources", ed. by Oleg A. Popov (Noyes Publications, Park Ridge, NJ), Chap. 1 (1995); UCLA PPG-1506 (1994).

[11] J.M. Pucci et. al., "Preliminary Characterization of a Helicon Plasma Source for Space Propulsion." AIAA 2006-5255. 42nd AIAA/ASME/SAE/ASEE Join Propulsion Conference and Exhibit, 2006.

[12] M. Celik and M. Martínez-Sánchez, "Experimental and Computational Studies of Electric Thruster Plasma Radiation Emission." Doctoral Thesis, Massachusetts Institute of Technology, 2007.

[13] O. Batishchev, J. Pucci, N. Sinenian, Z. LaBry, M. Celik, M. Martínez-Sánchez, "Mini-Helicon Thruster Experiment at MIT." QO1.4, 48th Annual Meeting of the Division of Plasma Physics, Philadelphia, PA, October 30November 3, 2006; Bulletin APS, 51 (7) 224, October 2006.

[14] O. Batishchev, Kinetic Model for the Variable Isp Thruster, Bull. APS , 44, 8, p. 99, 1999.

[15] M. Light and F.F. Chen, Helicon Wave Excitation with Helical Antennas, Phys. Plasmas **2**, 1084 (1995); UCLA PPG-1520 (1994).

[16] R.W. Boswell and F.F. Chen, Helicons, the early years, IEEE Trans. Plasma Sci. **25**, 1229 (1997).

[17] F.F. Chen and D. Arnush, Generalized theory of helicon waves I: Normal modes, Phys. Plasmas **4**, 3411 (1997); UCLA PPG-1562 (Aug 1996).

[18] F.F. Chen, X. Jiang, J.D. Evans, G. Tynan, and D. Arnush, Low Field Helicon Discharges, Plasma Phys. Control. Fusion **39**, A411 (1997); UCLA PPG-1564 (Sept. 1996).

[19] Bose et. al. Plasma Sources Sci. Tech. **13** 2004, 553-561.

[20] M. D. Carter et al., Physics of Plasmas, December 2002.

[21] J.A. Bittencourt, Fundamentals of Plasma Physics, 3rd Edition. Springer Press, 2004.

[22] I. H. Hutchinson. Principles of Plasma Diagnostics. Cambridge University Press, 2002.

[23] M. Celik et. al., Hybrid-PIC Simulation of a Hall Thruster Plume on an Unstructured Grid with DSMC Collisions., IEPC-03-134, 31st International Electric Propulsion Conference, 2003.

[24] O. Batishchev, Multi-Scale Modeling of Plasma Thrusters, NM2B.001, 46 APS DPP, Savannah, GA, November 18, APS Bulletin, 49, 8, p. 260, 2004.

[25] O. Batishchev, A. Batishcheva, A. Kholodov, Unstructured Adaptive Grid and Grid-free Methods for Edge Plasma Fluid Simulations, J. Plasma Phys. 61, 5, 1999, pp. 701-722.

[26] O. Batishchev, A. Batishcheva, RRC Adaptive Grid Method for Magnetized Plasma, Proceedings 17th Intl. Conf. On Numerical Simulation of Plasmas, 29, Banff, Canada, 2000.

[27] A. Batishcheva, O. Batishchev, Adaptive Kinetic Simulation of Plasma Propulsion by Laser Ablation, APS Bulletin, 49, 8, p. 260, 2004.

[28] B. Lawton and G. Klingenberg, Transient Temperature in Engineering and Science. Oxford University Press, 1996.

[29] D. Pollock, Thermocouples: Theory and Properties. CRC Press, 1991.

[30] M. N. Ozisik, Heat Conduction, 2nd Edition. John Wiley and Sons, Inc, 1993.

[31] J.I. Frankel, "Heat Flux Predictions From Surface Mounted Temperature Sensor With DFT and Filtering Analysis." IAC-05-C2.6.06, 2005.

[32] J.J. Bezuidenhout and J.A. Schetz, "Heat Flux Determination Using Surface and Backface Temperature Histories and Inverse Methods." AIAA 2001-3530. 37th AIAA/ASME/SAE/ASEE Join Propulsion Conference and Exhibit, 2001.

[33] www.accuratus.com, "Fused Silica." website, 2006.

[34] Y. Azziz and M. Martínez-Sánchez, "Instrument Development and Plasma Measurements on a 200-Watt Hall Thruster Plume." Masters Thesis, Massachusetts Institute of Technology, 2003.

[35] Naval Research Laboratory, NRL Plasma Formulary. NRL/PU/6790–06-491. Revised 2006.